



# EmbSAM: cell boundary localization and Segment Anything Model for fast images of developing embryos



Guoye Guan <sup>1,2,14</sup>, Cunmin Zhao <sup>3,14</sup>, Zelin Li <sup>4,5,14</sup>, Pei Zhang <sup>6</sup>, Yixuan Chen <sup>7</sup>, Pohao Ye <sup>3</sup>, Ming-Kin Wong <sup>3,11</sup>, Lu-Yan Chan <sup>3,12</sup>, Hong Yan <sup>4,5</sup>, Chao Tang <sup>7,8,9,13</sup> & Zhongying Zhao <sup>3,10</sup>

Cellular shape dynamics are critical for understanding cell fate determination and organogenesis during development. However, fluorescence live-cell images of cell membranes frequently suffer from a low signal-to-noise ratio, especially during long-duration imaging with high spatiotemporal resolutions. The low ratio is caused by a tradeoff between embryo viability and phototoxicity and photobleaching of fluorescent markers, which hinders effective cell shape reconstruction, particularly in rapidly developing embryos. Here, we devise an integrative computational framework, *EmbSAM*, that incorporates a deep-learning-based cell boundary localization algorithm and the Segment Anything Model. *EmbSAM* enables accurate segmentation of three-dimensional cell membrane images for roundworm *Caenorhabditis elegans* embryos imaged with exceptional temporal resolution, *i.e.*, every 10 seconds per stack. The resolved cell shapes prior to gastrulation quantitatively characterize a series of cell-division-coupled morphodynamics associated with cell position, cell division phase duration, cell division axis reorientation, cell identity, lineage, fate, among others, which can be accessed locally and online.

Embryogenesis is the developmental process during which a single-celled fertilized egg undergoes cleavage (rapid division) along with the emergence of stereotypical spatial architectures and fate maps of numerous cells, forming a functional larva that can survive independently<sup>1-3</sup>. The rapid division takes place concurrently with cell migration and cell differentiation, where cell shape changes dramatically to accommodate cell fate determination and organogenesis<sup>4,5</sup>. Studying detailed cellular behaviors during rapid division becomes a challenging task because early embryonic mitotic phases, during which three-dimensional (3D) cell shape changes drastically, are very short. In theory, fast (high-frequency) imaging is able to reconstruct the cellular behaviors, but it can only be conducted with a relatively lower laser power to minimize accumulative photobleaching and phototoxicity. Therefore, a more sensitive cell segmentation algorithm is needed to compensate for the low signal-to-noise ratio (SNR) of the acquired images<sup>6,7</sup>. For instance, the duration of cytokinesis, *i.e.*, the time between the complete

separation of sister cell nuclei and that of cell membranes, in early roundworm embryogenesis is roughly 2.5 min, during which the cell shape changes from spherical to dumbbell-shaped<sup>8,9</sup>. Notably, cytokinesis often exhibits differential behaviors (*e.g.*, differential cell division axes and durations of different phases of mitosis) along with specific cell shape dynamics depending on cell positions, cell identities, cell lineages, and cell fates. Moreover, these differential behaviors can also exist within a single cell type across successive cell cycles<sup>10-14</sup>. The details of cytokinesis and cell shape dynamics in such a short period are commonly missed in time-lapse 3D imaging due to insufficient spatial and temporal resolutions, especially the temporal one. Moreover, many cellular properties, in particular those related to cytokinesis, also change drastically over development, such as the asymmetric partition of cell volume between sister cells and the decrease of cell sphericity within roughly 7 min at late metaphase<sup>14,15</sup>. To enable illustration of the biological mechanisms underlying these cellular behaviors, it is

<sup>1</sup>Department of Systems Biology, Harvard Medical School, Boston, USA. <sup>2</sup>Department of Data Science, Dana-Farber Cancer Institute, Boston, USA. <sup>3</sup>Department of Biology, Hong Kong Baptist University, Hong Kong, China. <sup>4</sup>Department of Electrical Engineering, City University of Hong Kong, Hong Kong, China. <sup>5</sup>Centre for Intelligent Multidimensional Data Analysis Limited, Hong Kong Science Park, Hong Kong, China. <sup>6</sup>Department of Biology, Faculty of Arts and Sciences, Beijing Normal University, Zhuhai, China. <sup>7</sup>School of Physics, Peking University, Beijing, China. <sup>8</sup>Center for Quantitative Biology, Peking University, Beijing, China. <sup>9</sup>Peking-Tsinghua Center for Life Sciences, Peking University, Beijing, China. <sup>10</sup>State Key Laboratory of Environmental and Biological Analysis, Hong Kong Baptist University, Hong Kong, China. <sup>11</sup>Present address: Schulich School of Medicine and Dentistry, Western University, London, Ontario, Canada. <sup>12</sup>Present address: Department of Surgery, Chinese University of Hong Kong, Hong Kong, China. <sup>13</sup>Present address: Center for Interdisciplinary Studies, Westlake University, Hangzhou, China. <sup>14</sup>These authors contributed equally: Guoye Guan, Cunmin Zhao, Zelin Li. e-mail: [guanguoye@gmail.com](mailto:guanguoye@gmail.com); [zyzhao@hkbu.edu.hk](mailto:zyzhao@hkbu.edu.hk)

essential to acquire fluorescence images of cell membranes through time-lapse 3D live-cell imaging (also called *in toto* imaging) at an exceptional temporal resolution, which permits reconstruction of cell shape with sufficient temporal resolution to analyze cell shape dynamics during cytokinesis. Furthermore, cell shape reconstruction is crucial for quantifying the spatiotemporal dynamics of functional molecules associated with cell membrane and cell division, such as filamentous actin (F-actin) and non-muscle myosin (NMY) that control the cell cortex stiffness and fluidity<sup>12,16</sup>. However, because of photobleaching and phototoxicity, a tradeoff has to be applied between image quality and laser power or imaging frequency. This is especially true if both the cell identity and cell boundary need to be simultaneously resolved, with one laser channel for cell nucleus tracing and the other for cell membrane segmentation<sup>8,17</sup>. Therefore, the development of a cell (membrane) segmentation algorithm has to take into consideration a modest quality of fluorescence image, either for the raw one or the processed one.

The transparent roundworm *Caenorhabditis elegans* is one of the most popular models for studying the developmental control over embryogenesis due to its precise development, including cell lineage and fate, cell migration trajectory, cell division timing and axis orientation and cell size among others (Supplementary Fig. 1)<sup>18–24</sup>. Thus, multiple 3D cell segmentation algorithms that process time-lapse image stacks of different temporal resolutions have been devised in the past several years: *spheresDT/Mpacts-PiCS* at 3-min intervals<sup>25</sup>, *CShaper* at ~1.5-min intervals<sup>8</sup>, and *BCOMS2* at 30-s intervals<sup>15</sup>.

Apart from the customized frameworks, there are also many techniques developed for universal experimental conditions, in other words, for realizing the cell segmentation with a general computational framework, such as *CellProfiler*<sup>26</sup>, *RACE*<sup>27</sup>, and *SingleCellDetector*<sup>28</sup>. Recently, the Segment Anything Model (SAM) based on the Vision Transformer (ViT) architecture further revolutionized the field of computer vision, along with its truncated versions adapted to general 3D biomedical

images, *MedLSAM* and *MedSAM*<sup>29–33</sup>. The limitations of current SAM frameworks include their heavy reliance on manual input for segmentation promoters, such as seeding points or bounding boxes. Although the general SAM frameworks with these limitations may not be comparable to the customized ones when executed in the custom system (e.g., *spheresDT/Mpacts-PiCS*, *CShaper*, and *BCOMS2* for the *C. elegans* embryo<sup>8,15,25</sup>, they still impose a chance that the advantage of different approaches could be integrated so as to increase the overall cell segmentation performance coherently, for example, targeting the fluorescence images with a low SNR just like the ones obtained at a high temporal resolution and with a weak laser power<sup>9,20,21</sup>.

To realize cell-resolved shape reconstruction of developing embryos from fluorescence images with a low SNR, particularly those captured at high temporal resolutions on the order of 10 s or less, we devised *EmbSAM*, a computational framework that extends the SAM with additional cell boundary localization part containing a denoising module and a watershed module. This framework outputs 3D bounding boxes as a guide to direct the SAM to perform accurate segmentation of the cell membrane fluorescence in 2D, which can then be assembled in 3D space (Fig. 1). Evaluation using three *C. elegans* embryos imaged with a low SNR demonstrates that *EmbSAM* significantly outperforms *CShaper*, *MedSAM*, and *PlantSeg*, regarding 3D cell segmentation accuracy. Furthermore, *EmbSAM* was applied to segment six more *C. elegans* embryos imaged at 10-s intervals and up to the moment before gastrulation, leading to a quantitative measurement of cell shape changes for fundamental cellular behaviors (e.g., cell division and cell migration) as well as their dependence on cell positions, cell identities, cell lineages, and cell fates. The resulting data have been reformatted for both local and online analytical platforms previously made available to the public. Developmental landmarks such as post-fertilization pseudocleavage, dorsal-ventral and left-right body axes establishment, and spatial reorganization for gastrulation, are digitized and monitored over the course of time.

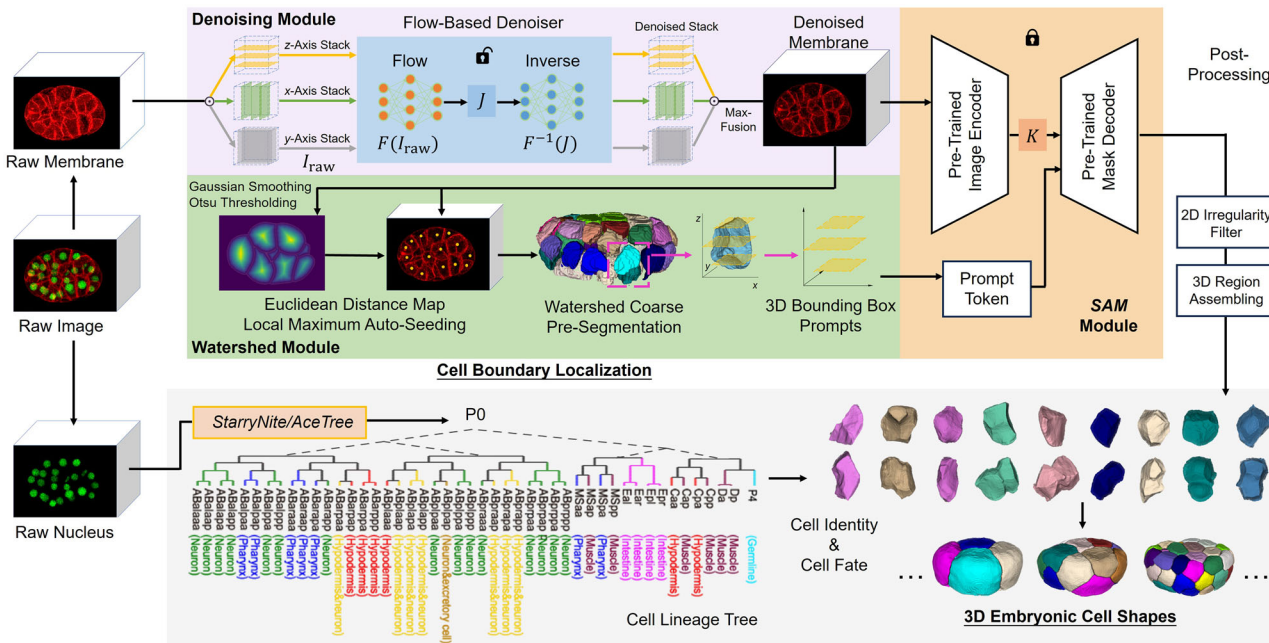


**Fig. 1 | The flowchart of *EmbSAM*, with time-lapse 3D fluorescence images (left) as input and lineage-resolved 3D cell shapes (bottom right) as output.** Top panel: Raw cell membrane fluorescence images were subjected to two add-on modules (denoising model highlighted with purple background and watershed module highlighted with blue background) that constitute the Cell Boundary Localization algorithm; the denoised images outputted by the denoising module are inputted into the image encoder in the SAM module<sup>30</sup>, while the watershed pre-segmentation outputted by the watershed module are inputted as the prompt tokens for the mask

decoder in the SAM module. The slice-by-slice segmentation results from the SAM module are subjected to 2D irregularity filter and 3D region assembling accordingly. Note that the lock icon represents frozen neural network without retraining and the unlock icon represents re-trained network with our data. Bottom panel: Raw cell nucleus fluorescence images were subjected to cell lineage tracing via *StarryNite/AceTree*<sup>50–52</sup>, where the outputted cell position and identity label each assembled 3D cell region.

## Results

### Performance of *EmbSAM* in cell segmentation on low-SNR images

With *C. elegans* wild-type embryo samples “Emb1” and “Emb2” at their 4-, 6-, 7-, 8-, 12-, 14-, 15-, 24-, 26-, 28-, and  $\geq 44$ -cell stages, we compared *EmbSAM* to *CShaper*<sup>8,17</sup> (one of the most updated algorithms customized for *C. elegans* embryonic images), *MedSAM*<sup>33</sup> (one of the most updated SAM algorithms generalized for biomedical images), and *PlantSeg*<sup>34,35</sup> (one of the most updated algorithms validated on both plant tissue and mouse embryonic images) (Supplemental Note 1). Considering that *MedSAM* was designed for segmenting 2D images and demands bounding box promoters to guide the reconstruction of 3D objects, the cell nucleus position ( $x_{\text{nuc}}, y_{\text{nuc}}, z_{\text{nuc}}$ ) and the conserved *C. elegans* embryonic cell volume ( $V$ )<sup>8,17</sup> documented before were utilized for constructing the required 3D bounding box promoters, a cuboid with boundaries  $(x_{\text{nuc}} \pm \sqrt[3]{\frac{3V}{4\pi}}, y_{\text{nuc}} \pm \sqrt[3]{\frac{3V}{4\pi}}, z_{\text{nuc}} \pm \sqrt[3]{\frac{3V}{4\pi}})$ ; therefore, the segmented 2D regions from *MedSAM* can be assembled into 3D regions.

In the *EmbSAM* segmentation, 99.73% of cells obtain fully connected 3D regions after the slice-by-slice 2D irregularity filtering. Intuitively, the *EmbSAM* segmentation outputs smooth and compacted cell shapes in both 2D and 3D for the whole embryo at developmental stages with a few to dozens of cells (Supplementary Fig. 2), while the segmented cell shapes from *CShaper*, *MedSAM*, and *PlantSeg* are coarse or uncompacted (Supplementary Fig. 3). While quantitative evaluation shows *PlantSeg* achieves a comparable performance to *EmbSAM* (reflected by Hausdorff distance) at the 12-cell stage, *EmbSAM* achieves both significantly larger Dice score ( $0.921 \pm 0.061$ ) and smaller Hausdorff distance ( $2.380 \pm 1.530$ ) than all *CShaper*, *MedSAM*, and *PlantSeg* at all developmental stages afterward<sup>8,17,33–35</sup>, supporting its outperformance in segmentation accuracy. Compared to the coarse or uncompacted cell shapes outputted by *CShaper*, *MedSAM*, and *PlantSeg*, the ones by *EmbSAM* resemble those of the ground truth (Fig. 2A). To test if *EmbSAM* holds its outperformance when image is even noisier, we further added artificial Poisson noise to each voxel: for each voxel with original fluorescence brightness  $\varphi_{(x,y,z)}$ , noise was sampled from a Poisson distribution with mean and standard deviation  $\sqrt{A\varphi_{(x,y,z)}}$ , where the amplification coefficient  $A$  took increasing values of  $0.01^*0$  (no noise),  $0.01^*0.75$ ,  $0.01^*0.5$ ,  $0.01^*0.25$ , and  $0.01^*0.1$ ; then all voxel brightness values were proportionally normalized to 0–255 (Supplementary Fig. 4). Across the first four noise levels, *EmbSAM* always achieved the largest Dice scores and smallest Hausdorff distances, while all algorithms failed at the highest noise level. This artificial noise experiment again demonstrates *EmbSAM*’s superior tolerance to noise and its high segmentation accuracy.

Apart from algorithm benchmarking, we further validated *EmbSAM*’s segmentation accuracy using the manually annotated ground truth from the additional embryo sample “Emb3” first published in this work (Supplementary Fig. 5). What is more, we inspected how reproducible *EmbSAM*’s segmentation accuracy is by segmenting the 3D image stack slice-by-slice along all six orthogonal axes (*i.e.*, with slicing direction along  $+x, -x, +y, -y, +z$ , and  $-z$ ), which is equivalent to rotating the stack while maintaining the original slicing direction along  $-z$ . With two embryo samples, 11 developmental stages, and 379 individual cells (Fig. 2B), we consistently observed large Dice scores ( $0.890 \pm 0.093$ ) and small Hausdorff distances ( $2.856 \pm 0.993$ ) and segmented 3D cell shapes matching ground truth and indistinguishable across all six conditions, confirming *EmbSAM*’s reproducible segmentation accuracy regardless stack rotation or slicing direction (Supplementary Fig. 6, and Supplementary Data 1).

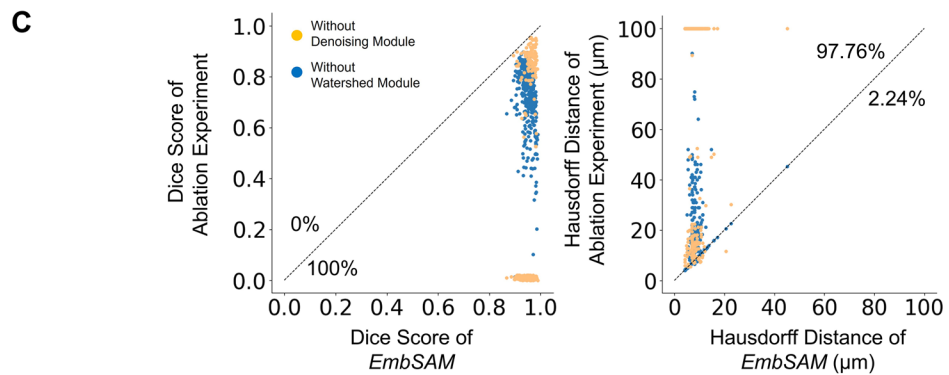
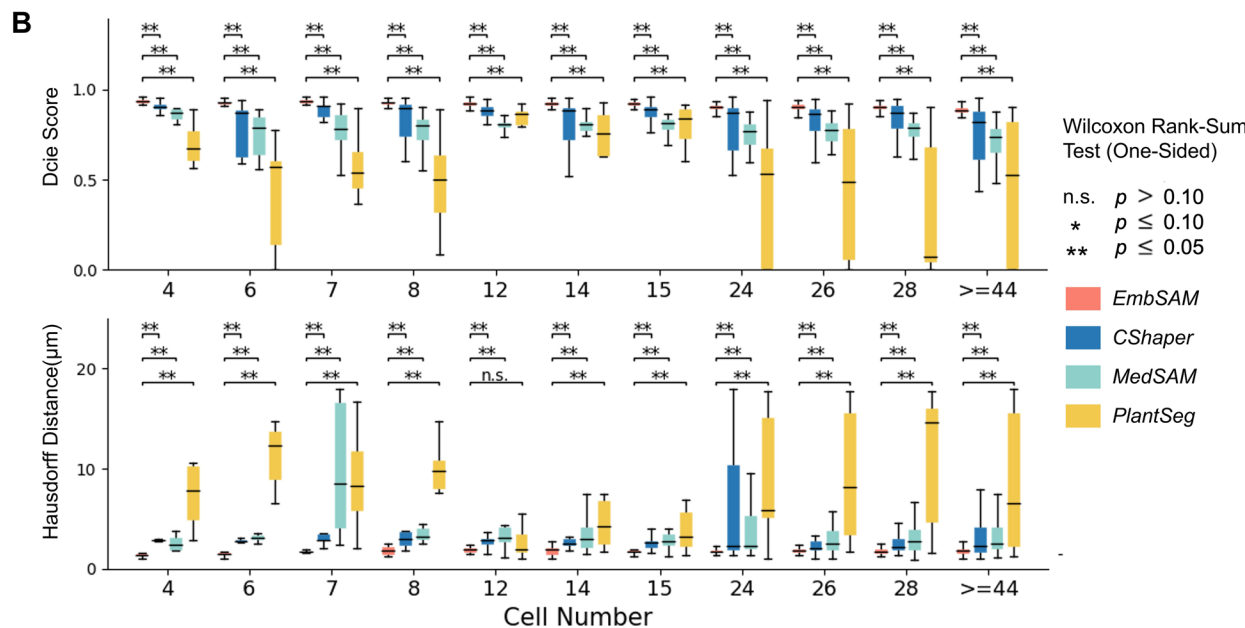
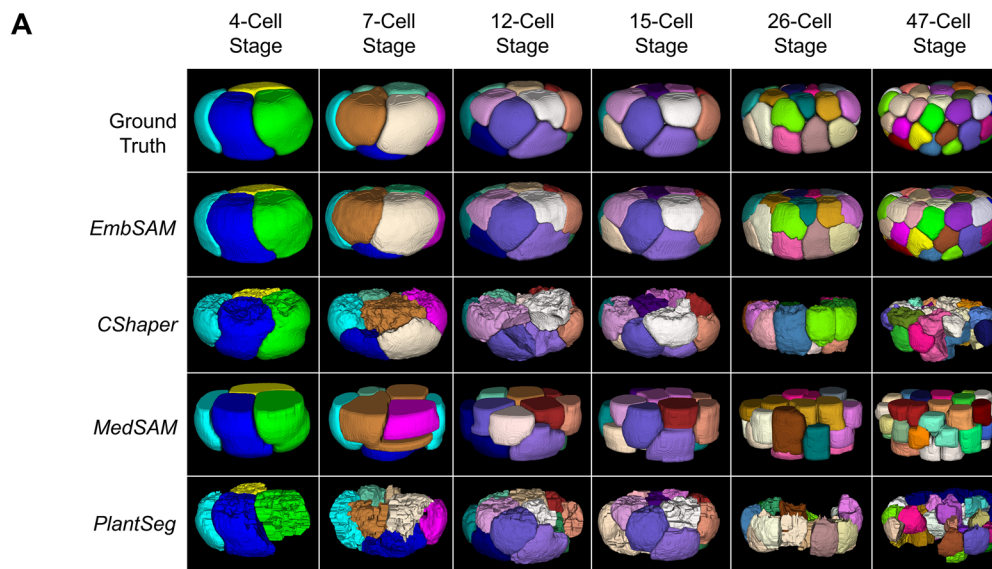
Further, we applied 3D shape descriptors (*incl.*, general sphericity, Hayakawa roundness, and spreading index) to assess cell shape consistency in three contexts: (1) between *EmbSAM* segmentation and ground truth; (2) across individual embryos (imaged under the same experimental condition with compression) segmented by *EmbSAM*; (3) between uncompressed and compressed embryos (imaged under the same experimental condition respectively) segmented by *EmbSAM*. First, shape descriptor values from

379 individual cells in “Emb1” and “Emb2” are highly similar between *EmbSAM* segmentation and ground truth (Supplementary Fig. 7;  $R = 0.993, 0.991, 0.996$  accordingly, with  $R^2$  from a proportional least-squares fit to test a proportional relationship), demonstrating considerable segmentation accuracy in terms of cell shape. Second, shape descriptor values in four embryo samples “Emb4” to “Emb7” (imaged under the same experimental condition with compression) are close to their averages (Supplementary Fig. 8;  $R = 0.851, 0.879, 0.753$  accordingly, with  $R^2$  from a proportional least-squares fit to test a proportional relationship). This suggests both the high accuracy of measurement and a tight control of *C. elegans* embryogenesis variability in the scale of cell shape, similar to cell lineage and fate patterns, cell division timings and axis orientations, cell cycle lengths, cell sizes (Supplementary Fig. 8;  $R = 0.952$  for volume and  $R = 0.932$  for surface area, with  $R^2$  from a proportional least-squares fit to test a proportional relationship), cell positions, and other cellular developmental properties discovered before<sup>8,18,36,37</sup>. It should be pointed out that the variation coefficients within *EmbSAM* segmentation (0.072 averaged over all 379 cells and three shape descriptors) and within ground truth (0.113 averaged over all 379 cells and three shape descriptors) are both low and near to each other, supporting both the high segmentation accuracy of our algorithm and the high biological reproducibility of embryogenesis. Third, all three shape descriptor values in compressed embryo samples “Emb4” to “Emb7” exhibit a decreasing trend in comparison to those in uncompressed embryos “Emb8” to “Emb9” (Supplementary Fig. 9). This overall cell shape shift raises enduring questions about how embryogenesis maintains robustness across varying mechanical environments, such as the compressive stresses experienced in aged or nutrient-deprived adults. Beyond local compensatory cell movements<sup>38</sup>, what global self-correction mechanisms are engaged to accommodate these variable cell shapes warrants further investigation, particularly using our dataset.

### Substantial contribution of denoising module and watershed module

To explain why *EmbSAM* and *MedSAM* (two SAM-based algorithms sharing the same segmentation architecture but differing in their training datasets) exhibit divergent performance, we evaluated the contributions of the denoising module and watershed module. To validate these modules’ effectiveness and necessity before SAM segmentation in the *EmbSAM* framework, we implemented an ablation experiment for each of them: when ablating the denoising module, the inputted image moves directly to watershed module and then segmentation module; when ablating the watershed module, the cuboid with boundaries  $(x_{\text{nuc}} \pm \sqrt[3]{\frac{3V}{4\pi}}, y_{\text{nuc}} \pm \sqrt[3]{\frac{3V}{4\pi}}, z_{\text{nuc}} \pm \sqrt[3]{\frac{3V}{4\pi}})$  surrounding the cell nucleus position is used as the 3D bounding box promoters (*i.e.*, SAM prompt tokens shown in Supplementary Fig. 10) for SAM segmentation of the image outputted by the denoising module. Besides, we added these modules individually and jointly into *MedSAM* before its SAM segmentation. The modified *MedSAM* produces smooth and compacted 3D cell shapes for  $\geq 44$ -cell-stage embryos, matching ground truth and appearing indistinguishable from *EmbSAM* (Supplementary Fig. 11). In both frameworks, omitting the denoising module led to severe cell missing, while omitting the watershed module led to unrealistic cell irregularity, underscoring their essential roles in mitigating low SNR and prompting cell boundary (generating slice-specific bounding boxes instead of *MedSAM*’s default rectangular 3D bounding box or 2D bounding box without automatic slice-specificity, which is yet to be refined<sup>33</sup> (Supplementary Fig. 12)) prior to SAM segmentation. These findings indicate that *EmbSAM*’s superior performance arises from its integrated denoising module and watershed module, while its segmentation module remains on par with other retrained SAM-based algorithms.

Quantitatively, the ablation experiments on *EmbSAM* reveal a global decline in segmentation performance following the removal of each module (Fig. 2C). While 97.76% of the 3D cell regions acquired a poorer Hausdorff distance after the denoising module removal, all of them acquired a poorer



Dice score. This evidence strongly supports the pivotal role of these two modules in recognizing individual cells in noisy images and promoting the accuracy of SAM segmentation. Such severe segmentation defects in ablation experiments were mostly seen at the top and bottom of the cells (Supplementary Fig. 11), where the fluorescence signal intensity is relatively lower due to the single-layer cell membrane (compared to the double-layer

ones formed by two contacting cells inside the embryo) and the loss of laser power through the  $z$ -axis (parallel to the imaging direction and perpendicular to the focal plane) in the embryo<sup>39,40</sup>.

While the classic watershed module was also used in some other cell segmentation algorithms customized for *C. elegans* embryonic images<sup>8,40–42</sup>, our denoising module was introduced to overcome the low SNR present in

**Fig. 2 | The segmentation performance of EmbSAM.** A Segmentation results (exemplified by the embryo sample “Emb1”) of ground truth (1<sup>st</sup> row), EmbSAM (2<sup>nd</sup> row), CShaper (3<sup>rd</sup> row), MedSAM (4<sup>th</sup> row), and PlantSeg (5<sup>th</sup> row) at different developmental stages. B Outperformance of EmbSAM compared to CShaper, MedSAM, and PlantSeg, revealed by Dice score (top) and Hausdorff distance (bottom). Presentation: box-and-whisker plot (colored interquartile with upper and lower quartiles as boundaries and median inside; whiskers extended to upper quartile + 1.5× interquartile range and lower quartile – 1.5× interquartile range; outliers beyond the range above). significance (one-sided Wilcoxon rank-sum test):

n.s. (not significant),  $p > 0.10$ ;  $^*p < 0.10$ ;  $^{**}p < 0.05$ ;  $^{***}p < 0.01$ . Data: the embryo samples “Emb1” and “Emb2” (*in toto*: 4-, 6-, 7-, 8-, 12-, 14-, 15-, 24-, 26-, 28-, and  $\geq 44$ -cell stage with 8, 12, 14, 16, 24, 28, 30, 48, 52, 56, and 91 data points, respectively, per embryo). C Poorer segmentation performance of EmbSAM when the denoising module and watershed module are ablated respectively, revealed by Dice score (left) and Hausdorff distance (right). The percentage of 3D cell regions with increasing or decreasing values is marked near the diagonal line. Data: the embryo samples “Emb1” and “Emb2” (*in toto*: 379 data points). Source data: Supplementary Data 5 for (B) and Supplementary Data 6 for (C).

certain images. To evaluate its performance in such a goal, we compared it with two other state-of-the-art image denoisers, *Noise2Void*<sup>43</sup> and *CARE*<sup>44</sup> (Supplementary Note 1), using the 2D image acquired at the mid-focal plane of embryo samples “Emb1” to “Emb 3” at their  $\geq 44$ -cell stage (Supplementary Fig. 13). Along the middle line  $y = 0$  (as a function of  $x$ ), our denoising module reaches a brightness distribution with zero regions at cytoplasm locations and sharp peaks at membrane locations, whereas *Noise2Void* exhibits noticeably lower contrast. At the embryo periphery, our denoising module yields continuous, uniform membrane fluorescence; in *CARE*-denoised images, the membrane signal appears thin and fragmented. These results demonstrate that our denoising module offers superior performance for low-SNR *C. elegans* embryonic images.

### Segmentation outperformance without reliance on cell nucleus information

While EmbSAM outperforms other membrane-based segmentation algorithms (*i.e.*, CShaper, MedSAM, and PlantSeg just compared), it remains to be seen whether EmbSAM can also outperform the nucleus-assisted ones. For *C. elegans* embryogenesis, this is a straightforward and useful strategy to prompt the segmentation of cell membrane boundary by providing the cell nucleus position as a seed<sup>39,40</sup>. In this context, CMap is a kind of such segmentation algorithm that very recently reconstructed a *C. elegans* morphological map with  $>95\%$  of embryonic cells segmented at 1.5-min intervals<sup>40</sup>. Thereof, we compare EmbSAM (only cell membrane fluorescence images) and CMap (using both cell membrane and cell nucleus fluorescence images, where the cell nucleus position is extracted and serves as a segmentation seed) as described above. Qualitatively, CMap outputs cell shapes resembling those of the ground truth, but they are coarser than both those of the ground truth and the ones by EmbSAM (Supplementary Fig. 14AB). Quantitatively, EmbSAM achieves both significantly larger Dice score and smaller Hausdorff distance than CMap at all developmental stages<sup>40</sup> (Supplementary Fig. 14C). These findings support EmbSAM’s outperformance in segmentation accuracy, and suggest that it more effectively discriminates cell membrane fluorescence signal from background noise, obviating the need for cell-nucleus-based seeding. By getting rid of the cell nucleus fluorescence channel, future experiments can repurpose that fluorescent label for other molecules of interest, such as the cell adhesion molecule E-cadherin (HMR-1), to quantify their dynamics in space and time with the segmented 3D cell shapes<sup>45</sup>.

### Monitoring 3D morphodynamics of cell biology event at 10-second intervals

Embryonic cell divisions proceed with drastic cell shape dynamics as fast as seconds to minutes, such as cytokinesis, which is coupled with rapid cell motion, asymmetric cell volume segregation, and fate differentiation<sup>10,11,13,14,21</sup>. Since the EmbSAM framework can effectively segment the cell membrane fluorescence images with a low SNR in the embryo samples “Emb1” to “Emb3” (Fig. 2, and Supplementary Figs. 2 and 5), we further applied it to other *C. elegans* wild-type embryo samples, “Emb4” to “Emb9”, that were imaged at a high temporal resolution but with a weak laser intensity<sup>9,20</sup>. Fascinatingly, the overall 3D cell shapes inside both embryos were successfully reconstructed up to the moment before gastrulation (*i.e.*, 24-cell stage) at 10-s intervals (Supplementary Movies 1 and 2), allowing a detailed study of specific cellular behaviors and developmental

landmarks with traced cell identities, lineages, and fates, as shown below<sup>46–48</sup>. Based on the four embryo samples with the most imaging time points, reconstruction process from the  $\leq 4$ - to  $\geq 24$ -cell stages requires  $<11$  h in total and  $<6$  min per time point on a GPU (graphics processing unit; NVIDIA A100 40 GB PCIe), demonstrating considerable computing efficiency for broad usage (Supplementary Data 2). Note that such smooth and compact cell shapes produced by our low-SNR fast imaging cannot be reconstructed by CShaper, which was originally customized for *C. elegans* embryonic images<sup>8,17</sup> (Supplementary Figs. 3 and 15). The digital embryonic cell shape data has been reformatted for convenient access, visualization, and analysis through public platforms, including both the local software *ITK-SNAP-CVE* and the online website <https://bcc.ee.cityu.edu.hk/cmos/embsam> (user instruction in Supplementary Movies 3 and 4)<sup>40</sup>.

### Cell shape dynamics related to cell division

The cell division axis orientation and cell cycle length have been known to be regulated by various biomechanical and biochemical processes<sup>10,13</sup>. Our segmented 3D cell shape data can illustrate the cell divisions in multiple lineages and generations at 10-s intervals, exemplified by the AB cells (the 1<sup>st</sup> somatic founder cell derived from the 1<sup>st</sup> cell division post fertilization) (Supplementary Fig. 16), EMS cell (the 2<sup>nd</sup> somatic founder cell derived from the 3<sup>rd</sup> cell division post fertilization) (Fig. 3A), MS and E cells (anterior and posterior daughter cell of EMS) (Supplementary Fig. 17), and C and P3 cells (the 3<sup>rd</sup> somatic founder cell and remaining germline stem cell derived from the 7<sup>th</sup> cell division post fertilization) (Supplementary Figs. 1 and 18). Each cell division is identified within a single segmented 3D cell region by a pair of mitotic sister cell nuclei (or two sets of separate reformed chromosomes after nuclear envelope breakdown) — distinct histone-labeled fluorescent domains — recognized via *StarryNite/AceTree* that comprises automatic tracing and manual correction<sup>49–52</sup>. Taking the EMS cell division for a case study, the Wnt signaling from its neighbor cell, *i.e.*, the P2 cell, controls its axis orientation and differentiation of the two daughter cells, *i.e.*, the MS cell for mesoderm and the E cell for endoderm<sup>53,54</sup> (Fig. 3A, and Supplementary Movie 5). Both the separation and motion of cell nuclei and cell membrane can be vividly visualized and quantitatively characterized, at the temporal resolution three times of the previous one<sup>15</sup> (Fig. 3A, and Supplementary Fig. 19). At the end of EMS cell division, in other words, the anaphase (starting with a symbol of cell nuclei separation and their widening gap), an increase of cell surface area is detected (Fig. 3B), in consistency with previous cell biology knowledge on cell division<sup>55,56</sup>. The cell sphericity keeps declining as reported before<sup>15</sup>, along with the other three independent cell shape descriptors (*i.e.*, Hayakawa roundness, spreading index, and diameter) obeying the same trend<sup>57</sup> (Fig. 3B). It is noteworthy that, the four embryo samples “Emb4” to “Emb7” shows lower variability in cell shape (with variation coefficient of 0.062, averaged over all five curves and all time points) is less than that of cell surface area and cell-cell contact areas (with variation coefficient of 0.342, averaged over all five curves and all time points), suggesting variability levels could substantially differ between cellular developmental properties even though they are essentially relevant (Fig. 3BC, and Supplementary Fig. 20).

The cell deformation with declining general sphericity, Hayakawa roundness, spreading index, and diameter during cell division is actually proceeding with the cell shape changed from spherical to dumbbell-shaped (Fig. 3A). Further exemplified by the ABpr and E cells and their neighbor

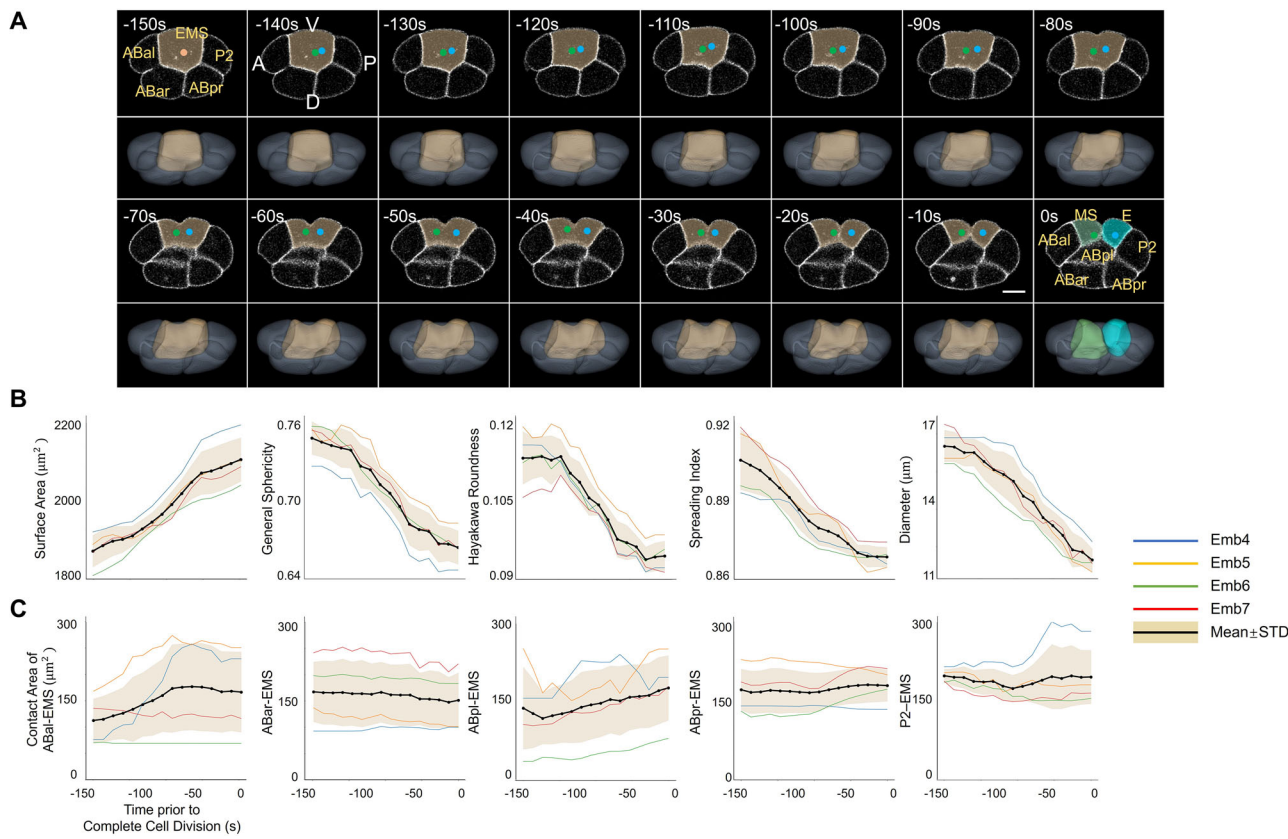


**Fig. 3 | The segmentation results (exemplified by the embryo sample “Emb5”) of EmbSAM for the EMS cell division at 10-second intervals. A** 2D (middle plane) and 3D segmentation results viewed in the imaging direction and highlighted by the dotted cell nuclei and masked cell membranes. Shown are lateral views with the anterior of the embryo to the left. All cell identities at the first and last moments are labeled next to their cell regions. Scarce bar: 10  $\mu$ m. **B** Monotonic curves of cell surface area, general sphericity, Hayakawa roundness, spreading index, and diameter over time, shown with their data in individual embryo samples (differentially color-

coded) as well as averaged over all embryo samples (black) alongside standard deviation (orange shade). **C** Curves of cell-cell contact area over time, shown with their data in individual embryo samples (differentially color-coded) and in average (black) with standard deviation (orange shade). For (A, B, C), the developmental time is shown, with the moment of complete cell membrane separation as time zero; For (B, C), the durations of all embryo samples are normalized to their average. Source data: Supplementary Data 7 for (B) and Supplementary Data 8 for (C).

cells (C and ABplp respectively), when a cell initiates its division program, it firstly turns spherical with its interface protruding toward its neighbor cell, and subsequently turns to dumbbell-shaped, squeezing its neighbor cell severely into a flat shape (Fig. 4A, B, and Supplementary Movies 6 and 7). Quantitative cell-cell contact interface curvature (defined as the reciprocal of radius of a sphere fitted to the curved contact interface) decreases continuously from positive values (indicating protrusion toward the dividing cell), through zero (indicating a flat interface), into negative values (indicating protrusion in opposite orientation to the initial one and toward the dividing cell’s neighbor<sup>58</sup>) (Fig. 4C, D). This implies a strong intracellular and intercellular mechanical force generated by the dividing cell. Such an intensive passive force and deformation exerted by a dividing cell on its neighbor cell appear to be a common phenomenon, further supported not only by the previously reported EMS and P2 cells (squeezed by ABa and ABp cell divisions) but also by other cells – C (squeezed by ABpl cell), ABplp (squeezed by E cell) (Fig. 4A, B), MS (squeezed by ABpl cell division), E (squeezed by ABpl cell division), among others<sup>58</sup> (Supplementary Figs. 21 and 22, and Supplementary Movie 8). Previous fluorescence imaging on the spatiotemporal dynamics of F-actin demonstrates its accumulation on the cell membrane near cell division and in the cytosol beyond cell division, which makes the cells get rounder and harder when it is around cell division (further validated by atomic force microscopy measurements of Young’s modulus)<sup>59</sup>. Our data can clearly illustrate such cell-cycle-dependent cell shape dynamics at 10-s intervals, represented by the cells mentioned above when they turn spherical and dumbbell-shaped

successively, squeezing their neighbor cells (relatively soft) to adapt to it (relatively hard) through severe deformation.

#### Cell shape dynamics related to body axis establishment

The anaphase and telophase of cell division, defined as starting from cell nuclei separation and ending in cell membrane separation, is as fast as 2.5 min measured before<sup>59</sup>. Such a short-term biological process is critical to establishing the body axes that determine the dorsal (D), ventral (V), left (L), and right (R) of an embryo (also called symmetry breaking), while the anterior-posterior (A-P) axis is determined by sperm entry and cell polarization that makes the first cell division asymmetric<sup>60,61</sup>. While the first two cells AB and P are located in the anterior and posterior of the embryo, respectively, the second cell division taking place in AB is initiated with an axis perpendicular to the A-P axis first and then reoriented to it, making its posterior daughter ABp determining the dorsal of the embryo (Fig. 5A, and Supplementary Movie 8).

As previous experimental observation indicated that the cell divisions in the AB lineage have a regulated reorientation during cytokinesis while the ones in the P1 lineage don’t<sup>11</sup>, we measure the skew angle of cell nuclei orientation during anaphase and telophase for all cells recorded (Fig. 5B), with each time-dependent curve averaged across embryo samples “Emb4” to “Emb7”. Here, the skew angle is quantitatively defined as the included angle between two vectors in 3D space: the first connects two cell nuclei at their initial separation (serving as the baseline at the first time point), and the second connects the same cell nuclei at any subsequent time point to track

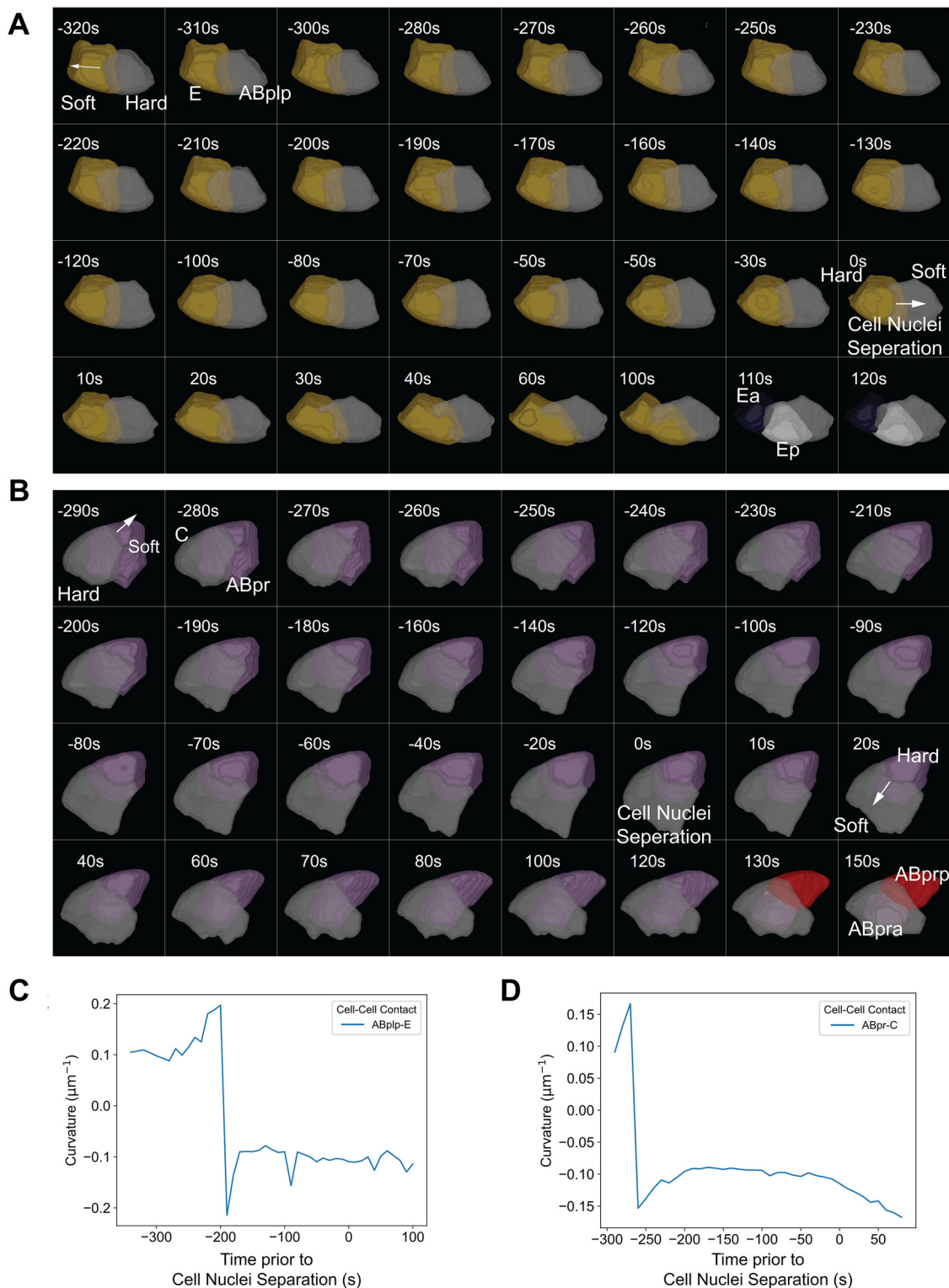


**Fig. 4** | The 3D segmentation results of *EmbSAM* for the drastic shape dynamics of dividing cells and newborn daughters (non-transparent), as well as their squeezed neighbors (semi-transparent) at 10-second intervals. **A** E cell division that squeezes ABplp, in accordance with Supplementary Movie 6. **B** ABpr cell division that squeezes C, in accordance with Supplementary Movie 7. The swapped cell-cell contact interface orientation originating from the hard cell and pointing the soft cell is highlighted by the starting and ending moments of the top three rows. For

(**A, B**), the developmental time is shown, with the moment of complete cell nuclei separation as time zero. **C, D** Curves of cell-cell contact interface curvature with sign changed over time, corresponding to (**A, B**) respectively. Data: the embryo sample “Emb5”. For (**A–D**), the developmental time is shown, with the moment of complete cell nuclei separation as time zero. Source data: Supplementary Data 9 for (**C**) and Supplementary Data 10 for (**D**).

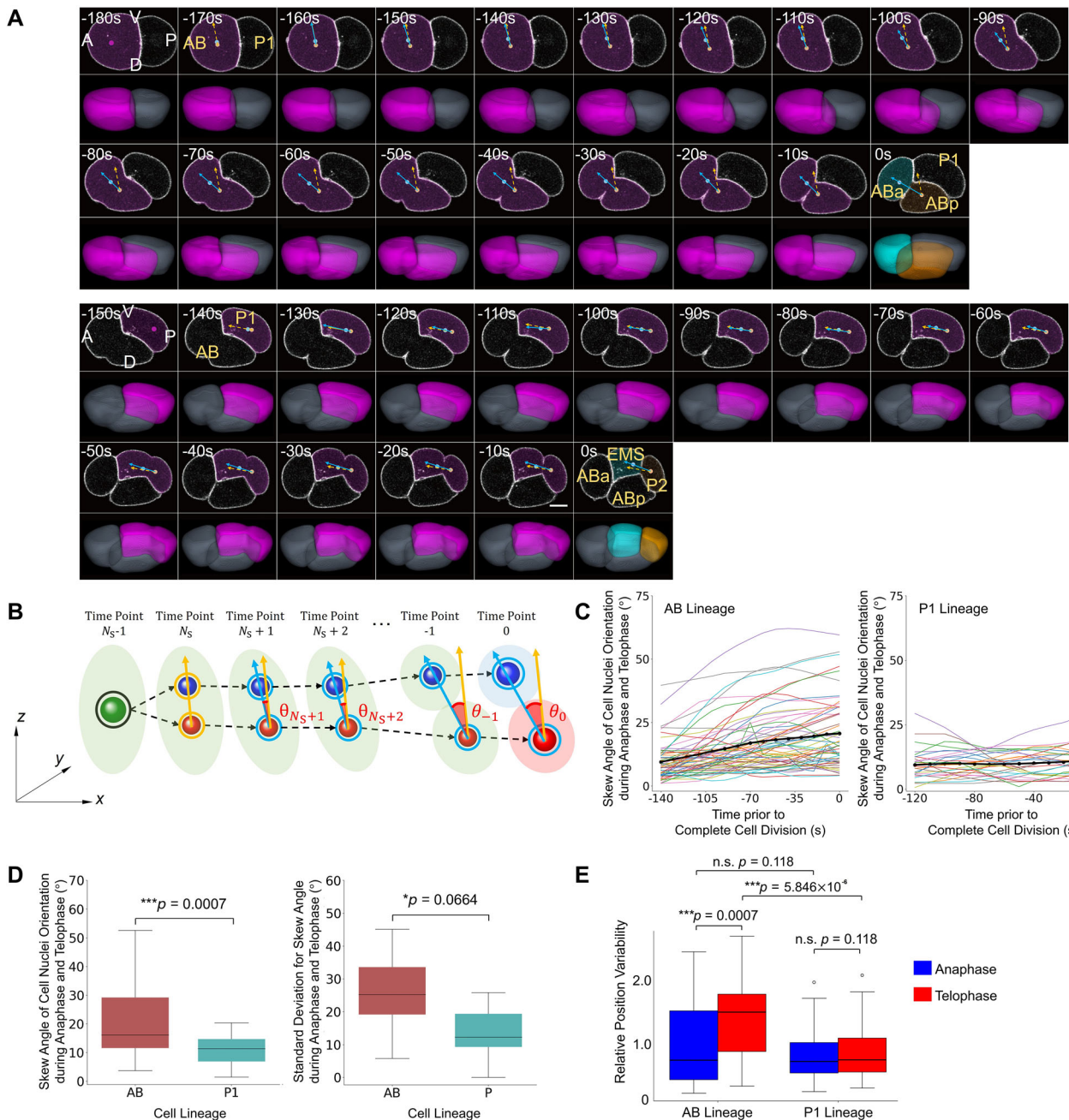


**Fig. 5 | The segmentation results (exemplified by the embryo sample “Emb5”) of EmbSAM for the cell division responsible for dorsal-ventral axis establishment at 10-second intervals. A** 2D (middle plane) and 3D segmentation results of the AB cell division (top, with the large skew angle of cell nuclei orientation) and P1 cell division (bottom, with the small skew angle of cell nuclei orientation), viewed in the imaging direction and highlighted by the dotted cell nuclei and masked cell membranes. Connecting lines between cell nuclei are overlaid on the time-lapse images: the dashed vector marks the initial separation orientation (serving as the baseline at the first time point), while the solid vector tracks subsequent orientation changes; the angle between these vectors in Cartesian coordinates quantifies the skew angle of cell nuclei orientation during anaphase and telophase. Shown are lateral views with the anterior of the embryo to the left. Scale bar: 10  $\mu$ m. **B** Intuitive schematic for how the skew angle of cell nuclei orientation during anaphase and telophase is calculated – the included angle between newborn cell nuclei’s connecting lines at the first moment (marked by  $N_S$ ) and later moments in Cartesian coordinates. **C** Curves of skew angle of cell nuclei orientation of all recorded cells in the AB lineage (left) and P1 lineage (right) over time. Data: the embryo samples “Emb4” to “Emb7” (*in toto*: AB and P1 lineages with 60 and 27 cells respectively). For (A–C), the developmental time is shown, with the moment of complete cell membrane separation as time zero; for (C) the durations of all embryo samples are normalized to their average.

**D** Comparison between all recorded cells in the AB lineage and P1 lineage, regarding their net skew angle of cell nuclei orientation during anaphase and telophase averaged over all embryo samples (left), and their standard deviation among all embryo samples (right). Presentation: box-and-whisker plot (colored interquartile with upper and lower quartiles as boundaries and median inside; whiskers extended to upper quartile + 1.5  $\times$  interquartile range and lower quartile – 1.5  $\times$  interquartile range; outliers beyond the range above). Statistical significance (one-sided  $t$ -test): n.s. (not significant),  $p > 0.10$ ; \* $p < 0.10$ ; \*\* $p < 0.05$ ; \*\*\* $p < 0.01$ . Data: the embryo samples “Emb4” to “Emb7” (*in toto*: AB and P1 lineages with 60 and 27 cells respectively). **E** Comparison between all recorded cells in the AB lineage and P1 lineage, regarding their positional variability at the onset of anaphase and at the end of telophase. Presentation: box-and-whisker plot (colored interquartile with upper and lower quartiles as boundaries and median inside; whiskers extended to upper quartile + 1.5  $\times$  interquartile range and lower quartile – 1.5  $\times$  interquartile range; outliers beyond the range above). Statistical significance (one-sided  $t$ -test): n.s. (not significant),  $p > 0.10$ ; \* $p < 0.10$ ; \*\* $p < 0.05$ ; \*\*\* $p < 0.01$ . Data: the embryo samples “Emb4” to “Emb7” (*in toto*: AB and P1 lineages with 10 and 6 cells respectively, per embryo). Source data: Supplementary Data 11 for (C) and Supplementary Data 12 for (D) and Supplementary Data 13 for (E).

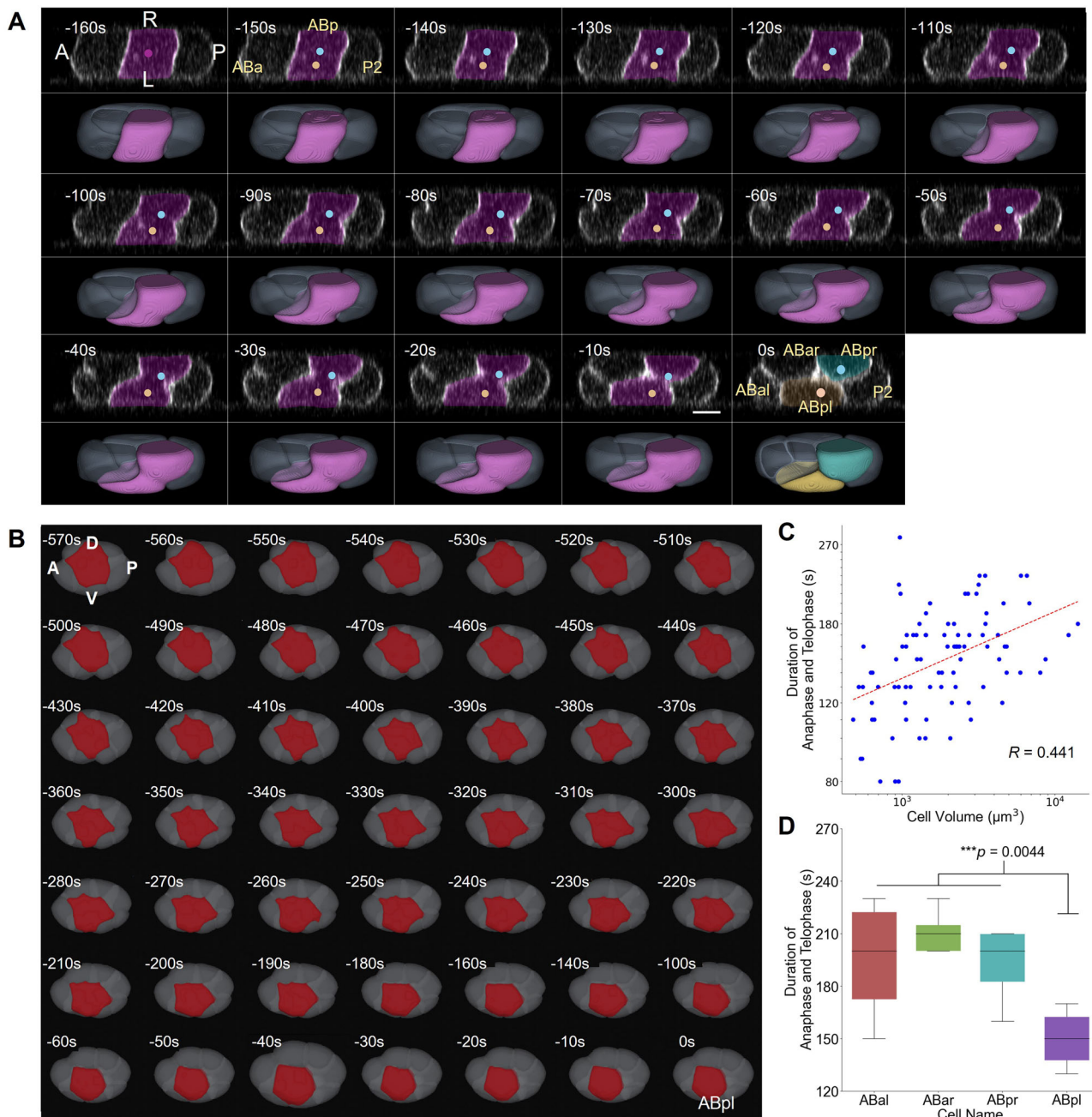


**Fig. 6 |** The segmentation results (exemplified by the embryo sample “Emb5”) of *EmbSAM* for the cell division responsible for left-right axis establishment at 10-second intervals. **A** 2D (middle plane) and 3D segmentation results of the ABp cell division, viewed from the dorsal view and highlighted by the dotted cell nuclei and masked cell membranes. Shown are lateral views with the anterior of embryo to the left. Scale bar: 10  $\mu\text{m}$ . The developmental time is shown, with the moment of complete cell membrane separation as time zero. **B** 3D segmentation results (exemplified by the embryo sample “Emb4”) of *EmbSAM* for the ABpl cell migration at 10-s intervals. Shown are lateral views with the anterior of the embryo to the left. ABpl is colored in red and other cells are in gray. The developmental time is shown, with the last moment before ABpl cell nuclei separation as time zero. **C** Positive correlation between cell volume and duration of anaphase and telophase (defined as starting from cell nuclei separation and ending in cell membrane separation as

illustrated in (A)). Data: the embryo samples “Emb4” to “Emb7” (*in toto*: 79 data points). **D** Significance comparison between ABpl cell and its sister and cousins (*i.e.*, the ABal, ABar, and ABpr cells), regarding the duration of anaphase and telophase (defined as starting from cell nuclei separation and ending in cell membrane separation as illustrated in (A)). Presentation: box-and-whisker plot (colored interquartile with upper and lower quartiles as boundaries and median inside; whiskers extended to upper quartile + 1.5 $\times$  interquartile range and lower quartile - 1.5 $\times$  interquartile range; outliers beyond the range above). Statistical significance (one-sided *t*-test): n.s. (not significant),  $p > 0.10$ ;  $^*p < 0.10$ ;  $^{**}p < 0.05$ ;  $^{***}p < 0.01$ . Data: the embryo samples “Emb4” to “Emb7” (*in toto*: 79 data points). Source data: Supplementary Data 14 for (C) and Supplementary Data 15 for (D).

orientation changes. Shown by the overall curve averaged over all cells at the temporal resolution of 10 s, the AB cells (*incl.*, AB, ABa, ABal, ABala, ABalp, ABalpa, ABalpp, ABar, ABara, ABaraa, ABarap, ABarp, ABarpa, ABarpp, ABp, ABpl, ABpla, ABplaa, ABplap, ABplp, ABpr, ABpra, ABpraa,

ABprap, ABprp, ABprpa, ABprpp) exhibit a stably increasing skew angle deviated from its initial direction but the P1 cells (*incl.*, EMS, MS, MSa, E, C, Ca, Cp, D, P1, P2, P3) exhibit a stably unchanged value, faithfully supporting previous conclusion (Fig. 5C). This conclusion holds whether the durations

of anaphase and telophase among embryo samples, along with the skew angle at those time points, are proportionally normalized to their length (leading to skew angle curves with an equal duration) or not (leading to skew angle curves with unequal durations) (Fig. 5C, and Supplementary Fig. 23). Although the AB cells carry substantially larger skew angle than P1 cells on average, their standard deviations among embryo samples is also larger (Fig. 5D). Alongside the more variable skew angle of AB cells, they also exhibit significantly higher positional variability (defined as root-mean-square deviation of distance vectors between a cell and all other cells, in all four embryo samples<sup>37</sup>) than P1 cells, at the end of the telophase but at the onset of anaphase (Fig. 5E). This finding suggests that, beyond the previously reported cell adhesion and gap junction<sup>37</sup>, regulated cell nuclei orientation skewing is another critical contributor to positional variability during embryonic development. In the future, the variability of skew angle, cell position, and other cellular developmental properties is worth joint investigation, using our data coupled with cell identities, cell lineages, and cell fates.

Following the diamond-shaped 4-cell stage with both anterior-posterior and dorsal-ventral symmetry breaking, the fourth and fifth cell divisions simultaneously taking place in ABa and ABp (anterior and posterior daughter of AB) are initiated with an axis roughly perpendicular to the plane constituted by the A-P and D-V axes; regulated by a contact-induced myosin flow demonstrated before<sup>10</sup>, the axis orientation is slightly skewed with the left daughter cells nearer to the anterior (Fig. 6A, and Supplementary Movie 9). Subsequently, the ABpl cell (left daughter of ABp) undergoes long-range migration toward the dorsal of the embryo with its migration-coupled spreading shape occurring in the middle of its lifespan<sup>45</sup> (Fig. 6B, and Supplementary Movie 10). The migration of ABpl, which has been identified with the longest distance among all cells before the 24-cell stage and has nearly the most irregular shape among all cells before the 350-cell stage<sup>8,20</sup>, was proposed to be driven by cell adhesion regulation<sup>9,62</sup> and enhances the left-right symmetry breaking substantially. Interestingly, the duration of anaphase and telophase positively associates with cell volume, evidenced in both absolute coordinates (Supplementary Fig. 24A;  $R = 0.300$ , with  $R^2$  from an unconstrained least-squares fit to test a power-law relationship) and semi-log coordinates (Fig. 6C;  $R = 0.441$ , with  $R^2$  from a proportional least-squares fit to test a proportional relationship). Although previous experimental measurements and our data consistently revealed that the cell cycle length negatively associates with cell volume<sup>21,63</sup> (Supplementary Fig. 24B), no correlation (Supplementary Fig. 24C,  $R < 0.001$ ,  $R^2$  from an unconstrained least-squares fit) was found between the cell cycle length and duration of anaphase and telophase. This is possibly attributed to the one-order-of-magnitude difference in their time-scales and distinct regulatory mechanisms without direct correlation: while cell cycle length is affected by the limited content of its regulatory molecules (e.g., nuclear pore complexes) unequally allocated during cell volume partition<sup>13,64</sup>, the duration of anaphase and telophase is likely affected by cell-volume-dependent physical constraints — namely, the distance sister nuclei must separate and the equatorial diameter that the contractile ring must ingress through during cytoskeleton remodeling for cytokinesis<sup>65,66</sup>.

The relationship between cell volume and the duration of anaphase and telophase appears in a global manner and independent of lineage: cells from both the germline lineage (i.e., P lineage) and all of its derived somatic lineages (i.e., AB, EMS, and C lineages, each with at least two cells) (Supplementary Fig. 1) intermix on both sides the fitted line, with no apparent shifts between lineages (Supplementary Fig. 24A). Notably, ABpl's duration of anaphase and telophase is significantly shorter than those of its sister and cousins with similar size (with a relative difference of <8%), probably reflecting its unique cytoskeletal state that facilitates left-right symmetry breaking and embryo rotation<sup>4,67</sup> (Fig. 6D). Beyond the difference between ABpl and its sister and cousins, the cell-specific duration of anaphase and telophase is reproducible between individual embryos. Remarkably, the unidentical cells' four duration lengths in embryo samples "Emb4" to "Emb7" (imaged under the same experimental condition with compression) fluctuate around their averages, which together considerably fit the

proportional relationship (Supplementary Fig. 24D;  $R = 0.767$ , with  $R^2$  from a proportional least-squares fit to test a proportional relationship) with a small variation coefficient of  $0.131 \pm 0.036$ . This suggests both the high accuracy of measurement and a tight control of *C. elegans* embryogenesis variability in the scale of cell division phase durations, similar to cell lineage and fate patterns, cell division timings and division orientations, cell cycle lengths, cell sizes (Supplementary Fig. 8;  $R = 0.952$ , with  $R^2$  from a proportional least-squares fit to test a proportional relationship), cell positions, and other cellular developmental properties discovered before<sup>8,18,36,37</sup>.

The 10-s window in our extensive dataset provides an opportunity to analyze the spatial distribution of functional subcellular structures (i.e., contractile ring, lamellipodia, protrusion, and filopodia) over time to understand the underlying mechanism for cell division and migration, how the dividing and migrating cells interact with their neighbors, and how are multidimensional cellular properties stored in our dataset (e.g., cell division, cell migration, cell shape, cell cycle, cell identity, cell lineage, cell fate, and cell nucleus position and size (Supplementary Fig. 25)) affect each other<sup>63,68</sup>. In the future, physical simulation of cytoskeletal dynamics is anticipated to elucidate their contributions to the cell division, migration, and deformation behaviors observed in this dataset<sup>69,70</sup>.

### Cell shape dynamics related to spatial reorganization for gastrulation

In addition to morphogenetic events driven by one or a few cell divisions, the ones proceeding over multiple rounds of cell divisions can also be characterized quantitatively at exceptional spatiotemporal resolutions. Previous experimental studies have reported that *C. elegans* early embryonic cells undergo spatial reorganization for gastrulation through apical-basal polarization, where all cells remain attached to the eggshell and form a cavity (blastocoel) to facilitate the upcoming cell ingress, i.e., gastrulation<sup>46,71</sup>. In our data with a temporal resolution of 10 s, the cells keep acquiring enlarged lateral contact area and slimmer shape to get aligned on the inner surface of the eggshell regularly (Supplementary Fig. 26A). This is supplemented by a strong negative correlation observed between the relative outer surface area (contacting the eggshell) of a cell and developmental time (Supplementary Fig. 26B).

### Conclusion

Quantitative and automatic reconstruction of time-lapse 3D cell shapes with fluorescently-labeled cell membranes is challenging, especially for a developing embryo, in which cells undergo rapid division and migration frequently coupled with cell fate specification and cell shape deformation. Such a challenge is even more severe when the fluorescence images exhibit a low SNR because of various experimental protocols (e.g., strains) and purposes (e.g., observing short-term or long-term biological processes) (Supplementary Fig. 27). In this paper, we successfully segmented the time-lapse 3D images with a relatively low SNR from nine *C. elegans* wild-type embryo samples with resolved cell identities, which had failed to be segmented by state-of-the-art algorithms. The successful segmentation is achieved by an integrative computational framework, *EmbSAM*, that contains a deep-learning-based denoising module and a watershed module followed by SAM, which allows accurate reconstruction of the cell shapes from multiple developing embryos (Figs. 1–3). With an exceptional temporal resolution as high as 10-s in six of the embryos, the results allow examination of the instantaneous change in cellular behaviors during rapid cell division of embryogenesis. For example, the cell shape change and nucleus movement during division and fast directional cell movement after division can be examined, together with their dependence on cell identities, cell lineages, and cell fates; upon those single-cell behaviors, whole-embryo morphogenesis including body axes establishment and spatial reorganization for gastrulation is illustrated in 3D, along with quantitative cellular properties like cell division axis reorientation and cell surface area distribution presented in the time course (Figs. 4–6). All the reconstructed time-lapse 3D cell shapes at 10-s intervals and calculated shape features (incl., cell volume, cell surface area, and cell-cell contact area) are publically available in the data

format of software *ITK-SNAP-CVE* and website <https://bcc.ee.cityu.edu.hk/cmos/embSAM><sup>40,72</sup>.

Given the high segmentation accuracy of the *EmbSAM* framework, it could be applied not only to the wild-type embryos but also to the perturbed ones, such as the one curated with external compression, laser ablation, and RNA interference, to uncover how a developing embryo coordinates cellular behaviors (*e.g.*, cell division and coupled motion) to enable the faithful formation of tissues or organs<sup>9,11,20,38,73,74</sup>. Preliminary test with fifteen more *C. elegans* wild-type and RNAi-treated embryos image reveals cell membrane segmentation is feasible with fluorescence labeling on alternative molecules, including both the homogeneously-distributed one (phosphoinositide) and the heterogeneously-distributed one (NMY-2), where the latter one (profiles biologically significant dynamics, *i.e.*, cell cortex fluidity associated with cell division and coupled motion)<sup>10–12</sup> could replace the traditional marker for cell membrane labeling and leave more fluorescence channels for monitoring the dynamics of other molecules simultaneously (Supplementary Note 2, Supplementary Figs. 28–31, and Supplementary Data 3). Such monitoring can be customized for specific developmental stages from fertilization to late and even post embryogenesis, for the whole body or tissue/organ of interest (*e.g.*, ACT-5 for monitoring the luminal formation in intestinal cells) (Supplementary Fig. 32) and at flexible intervals (*e.g.*, down to 2-s)<sup>75,76</sup> (Supplementary Fig. 33). Following this paradigm, more molecule dynamics in time-lapse format can be collected quantitatively by strain crossing, fluorescence imaging, and cell segmentation in a high-throughput manner. When imaging different fluorescent markers, variations in brightness or SNR will require fine-tuning of both laser power and re-trained denoising module; alternatively, for scenarios where cells lie in a 2D plane (*e.g.*, *C. elegans* 1- to 4-cell stages with anterior-posterior and dorsal-ventral axes establishment), image quality could be enhanced by projecting the z-stack into a 2D image for accurate cell membrane segmentation, revealed by embryos in the preliminary test (Supplementary Note 2, Supplementary Data 4, and Supplementary Figs. 28–31).

The fluorescence images of dozens of *C. elegans* embryos and the reconstructed cell shapes in 2D and 3D at high temporal resolutions in this work enable systematic, detailed, and in-depth analysis of cellular behaviors, including but not limited to the ones analyzed in this paper. For example, the skew angle of cell nuclei orientation during anaphase and telophase likely reflects both the cell nucleus movement inside a cell and the whole cell body's movement, where the orientation of a bounding box of the 3D cell body can be extracted by principal component analysis as demonstrated before<sup>57</sup>. Classic Hertwig's rule — namely, that how the embryonic cell division axis orientations are determined by cell nucleus movements, cell body movements, cell shapes, cell positions, cell-cell contact relationships and areas, as well as other external environments (*e.g.*, mechanical compression) and molecular dynamics (*e.g.*, myosin density and flow) — can be systematically investigated using our high-resolution multidimensional dataset<sup>10,12</sup>. The identified correlations, causal relationships, and independencies among these factors are expected to facilitate the construction of new theoretical models that help predict what's going on in reality. For instance, the cell shape change during fast cell division and cytokinesis can help understand the cell membrane mechanics, providing a reference for testing various cell membrane models established previously<sup>9,77–79</sup>. Moreover, such embryo-wide cell shapes can be used to reversely infer the intracellular and intercellular mechanical properties over development, which are usually hard to measure directly<sup>36,79–81</sup>. When replacing the fluorescent marker used for labeling cell membranes with those specific for other cellular or subcellular compartments (*e.g.*, E-cadherin and F-actin), the dynamics of their related cellular behaviors, such as cell adhesion and cell stiffness, can be examined with an exceptional temporal resolution, *i.e.*, at a 10-s or a shorter interval<sup>82,83</sup>. All the detailed cellular or subcellular behaviors above not only help understand the biological regulation *in vivo*, but also facilitate the establishment of a reliable, comprehensive computational model that simulates developmental control *in silico* and permits virtual experiments for mechanism discovery<sup>9,62,78,84</sup>. In the future, the *EmbSAM* framework could be used to analyze datasets with fluorescently-labeled cell

membranes beyond the ones analyzed in this work, such as those of ascidian, fruit fly, zebrafish, and mouse, so as to broaden the cell shape data in various biological contexts<sup>27,85,86</sup>.

In spite of the successful 3D segmentation of pre-gastrulating *C. elegans* embryos at 10-s intervals, performance declines at the periphery of embryos no matter they are mechanically compressed or not, leading to missing or overspreading cell regions (Supplementary Fig. 34). Estimated with representative embryo samples “Emb7” (under compression) and “Emb8” (without compression) in an 100-time-point intervals, those errors start occurring in the 500<sup>th</sup> time points, while the save duration up to the 400<sup>th</sup> time point ends with 22 cells for both embryos; between the 100<sup>th</sup> and 400<sup>th</sup> time points, the SNR of the 3D image volume (256 × 356 × 214 voxels, with a voxel resolution of 0.18 μm/pixel) was calculated to be just above 2, defining the quantitative image-quality threshold that *EmbSAM* can reliably deal with. The segmentation failure in embryo periphery is typical in *C. elegans* embryonic cell segmentation, stemming from the single fluorescent cell membrane layer at the edge, in contrast to the double layers between adjacent internal cells that boost intensity<sup>39,40</sup>. To extend data collection into later, more challenging periods of development, one may execute a two-stage imaging protocol – proceed the single channel (nucleus fluorescence) at 1.5-min intervals (minimizing photobleaching and phototoxicity while permitting cell lineage tracing) up to the 24-cell stage, and then switch to dual channels (nucleus and membrane fluorescence) at 10-s intervals with sufficient laser power<sup>87</sup>. On the computational front, cell segmentation algorithms could leverage spatiotemporal correlations between neighboring slices and consecutive frames (*e.g.*, short-term consistency in cell volume and shape) to improve accuracy and robustness, instead of completely separate segmentation slide-by-slide and frame-by-frame<sup>88</sup>.

## Methods

### Embryo data collection for time-lapse 3D cell segmentation

*C. elegans* is a well-established model animal cultured at laboratory for half a century. *C. elegans* is a hermaphrodite, which reproduces mostly through selfing although rare males are present and can mate with hermaphrodite<sup>89</sup>. A total of nine *C. elegans* wild-type embryo samples were used for 3D image acquisition and cell segmentation in this paper, with green fluorescence labeling cell nuclei and red fluorescence labeling cell membranes ubiquitously (strains ZZY0535 and ZZY0861)<sup>8,17,40</sup>. The images acquired according to the unified protocol<sup>8</sup> were subjected to cell segmentation. These fluorescence images exhibited a significantly lower SNR (quantification detailed in Section 2.5) than those successfully segmented by *CShaper* before<sup>90</sup> (Supplementary Fig. 35), preventing them from successful 3D cell segmentation by the *CShaper* (one of the most updated algorithms customized for *C. elegans* embryonic images), *MedSAM* (the most updated SAM algorithm generalized for biomedical images), or *PlantSeg* (one of the most updated algorithms validated on both plant tissue and mouse embryonic images) algorithm<sup>8,17,33–35</sup>. The fluorescence labeling on cell nuclei was used for cell lineage tracing (since no later than the 4-cell stage). This was conducted with *StarryNite* (automatic tracing) and with *AceTree* for visualization and manual correction<sup>50–52,91–93</sup>, which produced cell identity, division timing, and position to each cell in addition to assigning cell division. A total of nine embryos were imaged in 3D at two different temporal resolutions as described below.

Three embryo samples (strain ZZY0535)<sup>8,17</sup> were imaged at 1.41-min intervals for 60 time points, which were imaged in 712 × 512 pixels on the *xy* plane with a total of 68 focal planes along the *z*-axis (0.09 μm/pixel for the *xy* plane and 0.42 μm/pixel for the *z*-axis, *i.e.*, the imaging direction). Two of them were reused from our previous works<sup>20,21</sup>; these two embryo samples (“Emb1” and “Emb2”) were used for quantitatively evaluating the cell segmentation performance. The last embryo sample (“Emb3”) was first published in this paper, for further independent cell segmentation performance evaluation.

Two embryo samples (strain ZZY0535)<sup>8,17</sup> were imaged at 10-s intervals. One (“Emb4”) was published in our previous work<sup>20</sup>, which was imaged in 712 × 512 pixels on the *xy* plane with a total of 47 focal planes

along the  $z$ -axis (0.09  $\mu\text{m}/\text{pixel}$  for the  $xy$  plane and 0.59  $\mu\text{m}/\text{pixel}$  for the  $z$ -axis, *i.e.*, the imaging direction) for 260 time points. The other (“Emb5”) was published in our previous work<sup>9</sup>, which was imaged in  $712 \times 512$  pixels on the  $xy$  plane with a total of 47 focal planes along the  $z$ -axis (0.09  $\mu\text{m}/\text{pixel}$  for the  $xy$  plane and 0.59  $\mu\text{m}/\text{pixel}$  for the  $z$ -axis, *i.e.*, the imaging direction) for 300 time points. These two embryo samples exhibit cell cycle lengths strongly proportional to the ones in the embryo samples “Emb1” to “Emb3”, suggesting that the fundamental biological process was not affected by the imaging at a substantially higher temporal resolution (almost an order of magnitude) (Supplementary Fig. 27).

Another four embryo samples (strain ZZY0861)<sup>40</sup> were imaged at 10-s intervals for  $\geq 650$  time points, which were imaged in  $712 \times 512$  pixels on the  $xy$  plane (0.09  $\mu\text{m}/\text{pixel}$  for the  $xy$  plane). Two of them (“Emb6” and “Emb7”) were imaged with a total of 66 focal planes along the  $z$ -axis (0.46  $\mu\text{m}/\text{pixel}$  for the  $z$ -axis, *i.e.*, the imaging direction); another two of them (“Emb8” and “Emb9”) were imaged with a total of 56 focal planes along the  $z$ -axis (0.80  $\mu\text{m}/\text{pixel}$  for the  $z$ -axis, *i.e.*, the imaging direction). These four embryo samples (“Emb6” to “Emb9”) were used to reveal how the cell segmentation method will behave or fail at more challenging later stages of development.

It is worth noting that the four embryo samples “Emb4” to “Emb7” were imaged under mechanical compression according to the unified protocol<sup>8</sup>, whereas the two embryo samples “Emb8” and “Emb 9” were imaged without mechanical compression according to the unified protocol<sup>40</sup>. These two groups together will facilitate direct comparison of cell segmentation performance and embryonic development modes, while the former cohort itself can facilitate assessing developmental variability from embryo to embryo<sup>94,95</sup>.

### Manual annotation for ground truth

Manual annotation of cell membranes with fluorescence images was used as ground truth, which was necessary for training and evaluating an automatic cell segmentation algorithm. In this work, multiple groups of manually annotated ground truths were used as detailed below.

For training the deep-learning-based denoising module, 16 3D volumetric images manually annotated in five *C. elegans* wild-type embryos (a collection of 2339 3D cell objects) were adopted from our previous work; these manually annotated ground truths (binarized images showing ideal cell regions, used as the state after denoising), together with their corresponding raw images (noisy images with blurred cell regions, used as the state before denoising) with a SNR around 5.227, roughly twice the one of *EmbSAM* dataset (Supplementary Fig. 35), were generated through labor-intensive efforts and serve as a standardized and reusable resource for training a deep-learning-based denoising module<sup>8,90,96</sup> (Supplementary Data 4). Whether the denoising module trained with high-SNR images (*CShaper* dataset) is sufficient for dealing with low-SNR images (*EmbSAM* dataset) will be evaluated in subsequent analyzes (Supplementary Fig. 35). The 3D volumetric images were subsequently sliced in the  $x$ ,  $y$ , and  $z$  directions according to the corresponding recorded pixels, resulting in a total of 4096, 5696, and 2560 2D images, respectively. From these, we randomly selected 10% in each direction to construct the training dataset, which enabled comprehensive learning and adaptation, containing the imaging features on fluorescently-labeled cell shapes in different directions.

For evaluating the automatic cell segmentation performance, all the cell shapes of the embryo samples “Emb1” and “Emb2” at 4-, 6-, 7-, 8-, 12-, 14-, 15-, 24-, 26-, 28-, and  $\geq 44$ -cell stages (a collection of 379 3D cell objects) were meticulously annotated with respect to all the  $x$ ,  $y$ , and  $z$  directions, slice by slice and cell by cell. Besides, a total of 45 2D images (focal planes) in the embryo sample “Emb3” were manually annotated for independent performance evaluation.

### Embryo data collection for alternative fluorescently-labeled molecules

For time-lapse imaging, young adult worms were dissected to free embryos. The embryos were mounted on a 3–5% (wt/vol) agarose pad with 0.5% tetramisole and sealed with Vaseline. Green fluorescent protein (GFP) and

mCherry were visualized using 488 nm and 561 nm excitation lasers, respectively. Channels were imaged sequentially to eliminate bleed-through. Imaging in all channels was captured using 0.1-s exposure time and at 2- to 30-s intervals on an inverted spinning-disk confocal microscope (Olympus SpinSR10) using a Yokogawa CSU W1 scanner system, equipped with a  $60\times/1.4$  NA objective and two Hamamatsu ORCA Flash sCMOS cameras. All movies were acquired under the control of cellSens Dimension software (Olympus), in which multi- $z$  sections were merged into a single projected image using ImageJ<sup>97</sup>. Images were subsequently arranged using ImageJ with small and global adjustments for contrast and brightness. Embryos with fluorescence labeling the phosphoinositide through pleckstrin homology (PH) domain (“Emb10” to “Emb15”) and non-muscle myosin II (NMY-2) (“Emb16” to “Emb24”) are involved<sup>98–100</sup>.

For single-shot imaging, embryos were mounted in M9 buffer with 10 mM sodium azide (Sigma) on glass slides, and observed under the Carl Zeiss LSM 980 confocal microscope equipped with a Zeiss  $60\times/1.40$  NA oil immersion objective lens (Carl Zeiss). Lasers 488 nm were used to excite GFP. Single-plane images were taken as 6–10 sections along the  $z$ -axis at 0.2- $\mu\text{m}$  intervals. Multi- $z$  sections were acquired and merged into a single projected image using Zen software (Carl Zeiss). Images were subsequently arranged using Adobe Photoshop with small and global adjustments for contrast and brightness. Embryos with fluorescence labeling filamentous actin 5 (ACT-5) (“Emb25” to “Emb30”) are involved<sup>75,76</sup>.

### RNA interference

For standard RNA interference (RNAi), about 10 young adults were picked and cultured on RNAi plates (nematode growth media (NGM) containing 1 mM isopropylthiogalactoside (IPTG) and 100  $\mu\text{g}/\text{mL}$  ampicillin) seeded with bacterial clones of target genes, and their first-generation embryos were examined after 72 h. Worms were fed with RNAi bacteria containing the L4440 empty vector plasmid as a control treatment (EV RNAi). All RNAi clones were confirmed by sequencing. For time-lapse images, the young adult worms were put in the M9 buffer and dissected by two needles to release their embryos. Embryos were then mounted on a 2% agarose pad and imaged with oil immersion objectives.

### Signal-to-noise ratio evaluation for microscopy-produced cell membrane fluorescence image

For a 3D cell membrane fluorescence image  $I_{\text{raw}}(x, y, z)$  (with its brightness value  $\varphi(x, y, z)$  in each voxel  $(x, y, z)$  within the whole rectangular domain  $\Omega_{\text{whole}}$ ) produced by microscopy, 3D cell regions can be segmented either manually or automatically. To delineate the cell membrane domains, we inwardly erode each 3D cell region by five voxels in all directions; voxels present in the original region but absent after erosion define the membrane domain  $\Omega_{\text{membrane}}$ . Next, subtracting  $\Omega_{\text{membrane}}$  from  $\Omega_{\text{whole}}$  defines the background (cytoplasmic and extraembryonic space) domains  $\Omega_{\text{background}}$ . Finally, the fluorescence within  $\Omega_{\text{membrane}}$  (with voxel number  $N_{(x,y,z) \in \Omega_{\text{membrane}}}$ ) derives the average membrane signal:

$$\beta_s = \frac{\sum_{(x,y,z) \in \Omega_{\text{membrane}}} \varphi(x, y, z)}{N_{(x,y,z) \in \Omega_{\text{membrane}}}} \quad (1)$$

while the fluorescence within  $\Omega_{\text{background}}$  (with voxel number  $N_{(x,y,z) \in \Omega_{\text{background}}}$ ) derives the average background noise:

$$\beta_n = \frac{\sum_{(x,y,z) \in \Omega_{\text{background}}, \varphi(x,y,z) > 0} \varphi(x, y, z)}{N_{(x,y,z) \in \Omega_{\text{background}}}} \quad (2)$$

evaluating the SNR at the voxel resolution as  $\beta_{\text{R}} = \frac{\beta_s}{\beta_n}$ .

### Proposed cell segmentation framework

The proposed computational framework for cell segmentation, *EmbSAM*, consists of three major parts:

- The cell boundary localization part for denoising fluorescence images and generating bounding boxes for each cell region. This is primarily composed of a denoising module (the deep neural network that removes small noisy components to increase the SNR of raw images) and a watershed module (the pre-segmentation for generating bounding boxes based on a watershed algorithm and obtaining approximate boundaries of the target cell to be segmented)<sup>42,101</sup>.
- The SAM part for final automatic cell segmentation<sup>23</sup>. This accomplishes automatic cell segmentation based on a series of bounding box promoters. The SAM module maximizes the performance of the proposed framework, whose pre-trained model was trained with billions of images containing thousands of imaging conditions. It is one of the reasons that it probably can help deal with low-SNR images. For the target cells in each slice (focal plane), the bounding box produced by the cell boundary localization part was used to facilitate the SAM segmentation with 3D assembling.
- The cell tracing part for assigning cell identity to the reconstructed 3D cell regions. The cell nucleus position output by *StarryNite* and *AceTree* is used to match its corresponding 3D cell region.

### Image denoising using conditional normalizing flow

The image-denoising network is based on the *LLFlow* (Low-Light Image Enhancement with Normalizing Flow) model<sup>101</sup>, which utilizes a conditional normalizing flow model<sup>102,103</sup> informed by the Retinex theory<sup>104</sup>. The workflow of step-by-step data processing and network training in this module is detailedly described in Supplementary Fig. 36 and Supplementary Note 3. Given a raw image  $I_{\text{raw}}$ , the processing procedure includes histogram equalization, color extraction, and noise extraction followed by the *RRDB* (Residual-in-Residual Dense Block) module<sup>105</sup> for feature extraction, resulting in the illumination invariant color map  $G(I_{\text{raw}})$ . The trained invertible network  $F$  of the conditional normalizing flow can construct the transformation process of the probability distribution between the manually annotated ground truth image with low noise ( $I_{\text{clean}}$ ) and its original cell membrane fluorescence image with high-noise ( $I_{\text{raw}}$ ) from a latent code  $J$  that aligns with the standard Gaussian distribution and  $G(I_{\text{raw}})$ . Here,  $F$  consists of three layers (*incl.*, a squeeze layer and 12 flow steps), with the probability density function  $P(I|I_{\text{ref}})$  in the condition (reference image) of  $I_{\text{ref}}$  expressed as:

$$P(I|I_{\text{ref}}) = \frac{1}{2b} \exp\left(-\frac{|I - I_{\text{ref}}|}{b}\right) \quad (3)$$

where  $b$  is a positive constant related to the learning performance. Thus, the probability distribution of  $I_{\text{clean}}$  under the condition of  $I_{\text{raw}}$  can be represented as  $P(I_{\text{clean}}|I_{\text{raw}})$ , and the transformation process can be represented as  $I_{\text{clean}} = F(J, I_{\text{raw}})$ . From the established conditions, we can derive  $\int P(I_{\text{clean}}|I_{\text{raw}}) \partial I_{\text{clean}} = \int P(J|I_{\text{raw}}) \partial J$  and  $J = F^{-1}(I_{\text{clean}}, I_{\text{raw}})$ . After applying the Jacobian correction to the probability density of  $J$ , we obtain:

$$P(I_{\text{clean}}|I_{\text{raw}}) = P_J(J|I_{\text{raw}}) \left| \frac{\partial F^{-1}(I_{\text{clean}}, I_{\text{raw}})}{\partial I_{\text{clean}}} \right| \quad (4)$$

To capture distributional differences between noise and cell features, a negative log-likelihood (NLL) minimization approach is utilized to maximize the probability distribution of  $P(I_{\text{clean}}|I_{\text{raw}})$  to train  $F$ , getting the loss function:

$$\begin{aligned} \text{Loss}(I_{\text{raw}}, I_{\text{clean}}) = -\log(P(I_{\text{clean}}|I_{\text{raw}})) = -\log P_J(J|I_{\text{raw}}) \\ - \log \left| \frac{\partial F^{-1}(I_{\text{clean}}, I_{\text{raw}})}{\partial I_{\text{clean}}} \right| \end{aligned} \quad (5)$$

After training, the inference can be implemented onto all raw images beyond the manually annotated ground truths,  $\hat{I}_{\text{clean}} = F(J, I_{\text{raw}})$ , deriving their low-noise outputs (Fig. 1, and Supplementary Fig. 37).

During denoising, 2D images are stacked along the  $z$ -axis to construct a 3D image resized to (256, 356, 160) by trilinear interpolation with an even

voxel resolution of  $0.18 \mu\text{m}/\text{pixel}$ . Then 2D slices are generated by cutting the 3D images along the  $x$ -,  $y$ -, and  $z$ -axis, followed by the denoising process in all three directions. For each pixel in space, the maximum value from its three orthogonal denoised 2D slices is adopted, so that a small-noise 3D image is recombined. This denoising step is essential for taking advantage of the complementary information in three directions regarding the 3D cell membrane fluorescence images.

### Auto-seeding watershed pre-segmentation for generating bounding box promoter and locating cell boundary

The denoised volume (3D image) is fed into the watershed module for generating bounding box promoters that approach cell boundaries slice-by-slice. The workflow of step-by-step data processing in this module is detailedly described in the middle row of Fig. 1. A Gaussian filter is applied for image smoothing, utilizing a Gaussian kernel size of 13 and a standard deviation of 2. The image is binarized via Otsu's thresholding<sup>106</sup> to produce  $M$ , producing an intermediate 3D image,  $M$ , in which  $C$  and  $E$  represent the pixels valued 0 (cell interior and exterior) and 1 (cell boundary) respectively. Then, the watershed pre-segmentation algorithm<sup>41</sup> from our previous work<sup>8,42</sup> was applied on  $M$ . The 3D Euclidean distance map of  $M$  is obtained:

$$Ed(x, y, z) = \min_{(x, y, z) \in C} \left\{ \min_{(x_0, y_0, z_0) \in E} \left\{ (x - x_0)^2 + (y - y_0)^2 + (z - z_0)^2 \right\}, 10 \right\} \quad (6)$$

Delaunay triangulation is executed on the local maximum in  $Ed$  (potential cell centers), where the edge  $e_{ij}$  between vertices  $i$  and  $j$  is assigned a weight by accumulating the  $Ed$  values along  $e_{ij}$ :

$$W_{e_{ij}} = \sum_{(x, y, z) \in e_{ij}} Ed(x, y, z) \quad (7)$$

Here, vertices with an edge having a  $W$  value below a threshold (numerical value: 10, with a unit of pixel in the resized 3D image, corresponding to a length of  $1.8 \mu\text{m}$  in reality; empirically customized for *C. elegans* embryonic images by previous independent research<sup>42</sup>) are clustered as the centers inside the same cell. The vertex clusters (seeding points) and the Euclidean distance map are inputted into the watershed algorithm<sup>107</sup>, marking both foreground (cell interior) and background (cell exterior) regions. It is worth pointing out that the local maximum is used to find seeds rather than the traced cell nucleus position, which makes *EmbSAM* segmentation fully independent of the cell nucleus fluorescence and allows for future adaptation to an alternative fluorescent label (replacing the cell nucleus fluorescence channel in microscopy) on a molecule of interest (e.g., E-cadherin or HMR-1 that controls cell adhesion), enabling quantification of its spatiotemporal dynamics on top of the segmented 3D cell shapes<sup>45</sup>. Upon completion of these steps, the binary image with only the embryo interior and exterior is converted into the one with distinct 3D cell regions (Fig. 1, Supplementary Fig. 37). For each  $z$  slice in a pre-segmented 3D cell region, the rectangle enclosing its 2D cell region (represented as  $[x_{\min} : x_{\max}, y_{\min} : y_{\max}, z_{\min} : z_{\max}]$ ) forms a series of 2D bounding box promoters for the following SAM module.

### Segment Anything Model

For each time point, both the denoised 2D images (automatically disassembled from the denoised volume along  $z$ -axis) and all the 2D bounding boxes surrounding a specific cell outputted by the watershed module were fed into the pre-trained zero-shot SAM (base vision model named *vit\_b*)<sup>30</sup>. The segmentation output of SAM is a 3D cell region comprising both background (0, cell exterior) and foreground (1, cell interior). The workflow of step-by-step data processing in this module is detailedly described in Supplementary Fig. 10.

When performing cell segmentation, the SAM module might generate multiple potential 2D regions within the same area, including noises, the target cell, or its neighboring cells. Here, we selected the largest area as the

target cell region. Additionally, unreasonable irregular regions such as dispersed coraloid or starlike shapes need to be filtered, especially around the embryo's top and bottom cell periphery where noise is higher (since the membrane lies parallel to the confocal plane and has only one single fluorescent layer) (Supplementary Fig. 38). To this end, we calculated the nondimensional irregularity of each 2D cell region,  $\eta = \frac{c}{\sqrt{s}}$ , where  $c$  and  $s$  represent its circumference and surface area respectively. For calculating a 2D cell region's perimeter, we used the Douglas-Peucker algorithm for contour approximation, with the approximation coefficient set as 0.01<sup>108</sup>. By analyzing the irregularity of 265,704 manually annotated 2D cell regions in two previous independent research<sup>8,40,90,96</sup>, a threshold (numerical value: 9.02, with no unit) was obtained for establishing a reasonable range for 2D cell irregularity at the 99% confidence (Supplementary Fig. 39). After slice-by-slice filtering by the cell irregularity threshold, all the remaining reliable 2D regions of a target cell are assembled into 3D, reconstructing cell-identity-resolved shapes with their cell-lineage-tracing information.

## Cell segmentation performance evaluation

To systematically assess the similarity between the cell segmentation results and their ground truth annotations, we adopted two widely recognized metrics for 3D object comparison<sup>109,110</sup>:

- Dice score: The ratio of the overlapping volume to the total volume of two 3D objects.
- Hausdorff distance: The maximum distance calculated from every voxel in one 3D object to its nearest voxel in another 3D object.

In theory, a larger Dice score and a smaller Hausdorff distance indicate a higher consistency between the cell segmentation results and their ground truth annotations.

## 3D cell shape descriptor

The characteristics of cell shapes enclosed by their segmented cell membranes can be quantitatively described by a series of 3D shape descriptors with explicit geometric significance. Here, we adopted three 3D cell shape descriptors from our previous work as follows<sup>57</sup>:

- Taking a perfect sphere with the same volume as the cell, “*general sphericity*” is defined as the ratio of its surface area to that of the cell, in other words, it describes the similarity of the cell to a perfect sphere<sup>111,112</sup>:

$$\text{General Sphericity} = \frac{\sqrt[3]{36\pi V^2}}{S} \quad (8)$$

where  $V$  and  $S$  are the volume and surface area of the cell respectively

- While “*general sphericity*” assesses the gross shape of a cell, “*Hayakawa roundness*” specifically assesses the sharpness of edges and corners, as well as the presence of the convexities and concavities on the cell surface<sup>112,113</sup>:

$$\text{Hayakawa Roundness} = \frac{V}{S\sqrt[3]{abc}} \quad (9)$$

where  $a$ ,  $b$  and  $c$  are the length of the long, intermediate, and short axes of the oriented bounding box (OBB) of the cell, respectively, estimated by principal component analysis<sup>112,114</sup>.

- Derived from a 2D definition, “*spreading index*” reflects the degree to which the convex hull of a cell resembles a perfect sphere, *i.e.*, the spreading of the cell shape<sup>115,116</sup>:

$$\text{Spreading Index} = \frac{\sqrt[3]{36\pi V_{\text{convex}}^2}}{S_{\text{convex}}} \quad (10)$$

where  $V_{\text{convex}}$  and  $S_{\text{convex}}$  are the volume and surface area of the convex hull enclosing the cell, respectively.

- During cytokinesis, the mother cell nucleus divides into two daughter cell nuclei with locations  $(x_{\text{nuc1}}, y_{\text{nuc1}}, z_{\text{nuc1}})$  and  $(x_{\text{nuc2}}, y_{\text{nuc2}}, z_{\text{nuc2}})$ ; almost at the same time, the cell membrane elongates with the equatorial plate ingressing as a contractile ring, whose diameter keeps shrinking<sup>117</sup>. The equatorial plate with a contractile ring is presumed as perpendicular to the line between the two daughter cell nuclei. Hence, the plane equation is described by  $(Ax + By + Cz + D = 0)$ , where  $(A, B, C) = (x_{\text{nuc2}} - x_{\text{nuc1}}, y_{\text{nuc2}} - y_{\text{nuc1}}, z_{\text{nuc2}} - z_{\text{nuc1}})$  is its normal vector defined by the positions of the two daughter cell nuclei and  $D$  is determined as follows. All pixels with a distance to the plane smaller than 0.5 pixels form an approximate cylinder with a height of 1 pixel, by which the diameter of the contractile ring can be derived from its surface area:

$$\text{Diameter} = 0.18 \text{ } \mu\text{m} \times \left( \sqrt{1 + \frac{2S_{\text{cylinder}}}{\pi}} - 1 \right) \quad (11)$$

where  $S_{\text{cylinder}}$  is the surface area of the convex hull enclosing the cylinder and  $D$  is determined by searching the smallest  $S_{\text{cylinder}}$ .

## Statistics and reproducibility

The time-lapse 3D data studied for statistics and reproducibility in this work was produced by an experimental-computational pipeline, which incorporates time-lapse 3D fluorescence imaging, cell-nucleus-based lineage tracing<sup>50-52</sup>, cell-membrane-based shape reconstruction, and 2D-irregularity-based region filter for *C. elegans* embryos (Methods). No data were excluded in the following quantitative analyzes.

Three groups of *C. elegans* embryo samples with time-lapse 3D shape reconstruction were used for statistics and reproducibility study: compressed embryos imaged at 1.41-min intervals (“Emb1” and “Emb2”), compressed embryos imaged at 10-s intervals (“Emb4” to “Emb7”), uncompressed embryos imaged at 10-s intervals (“Emb8” and “Emb9”). Wherever statistics or reproducibility is studied, data from all embryos within each group were used systematically and unbiasedly.

All quantitative results are supported by significance values for statistics and at least two replicates for reproducibility, corresponding to the sample size used in previous developmental biology and spatial patterning research<sup>118,119</sup>.

## Reporting summary

Further information on research design is available in the Nature Portfolio Reporting Summary linked to this article.

## Data availability

Source data for quantitative and statistical analyses in Fig. 2B (Supplementary Data 5), Fig. 2C (Supplementary Data 6), Fig. 3B (Supplementary Data 7), Fig. 3C (Supplementary Data 8), Fig. 4C (Supplementary Data 9), Fig. 4D (Supplementary Data 10), Fig. 5C (Supplementary Data 11), Fig. 5D (Supplementary Data 12), Fig. 5E (Supplementary Data 13), Fig. 6C (Supplementary Data 14), Fig. 6D (Supplementary Data 15), Supplementary Fig. 4 (Supplementary Data 16), Supplementary Fig. 7 (Supplementary Data 17), Supplementary Fig. 8 (Supplementary Data 18), Supplementary Fig. 9 (Supplementary Data 19), Supplementary Fig. 14 (Supplementary Data 20), Supplementary Fig. 20 (Supplementary Data 21), Supplementary Fig. 23 (Supplementary Data 22), Supplementary Fig. 24 (Supplementary Data 23), Supplementary Fig. 26 (Supplementary Data 24), Supplementary Fig. 27 (Supplementary Data 25), Supplementary Fig. 35 (Supplementary Data 26), and Supplementary Fig. 39 (Supplementary Data 27) are provided in Supplementary Data (accessible via <https://doi.org/10.6084/m9.figshare.29064530>). The raw, manually annotated, and processed images, as well as all the reconstructed time-lapse 3D cell shapes at 10-second intervals and calculated shape features (*incl.*, cell volume, cell surface area, and cell-cell contact relationship and area) in the readable data format of software *ITK-SNAP-CVE*, are accessible via <https://doi.org/10.6084/m9.figshare.29064530>.

29064530; the software *ITK-SNAP-CVE* is also accessible via <https://doi.org/10.6084/m9.figshare.29064530>. Alternatively, these equivalent reconstructed cell shape data can be browsed using the online website <https://bcc.ee.cityu.edu.hk/cmos/embSAM>. Supplementary Movie 3 and Supplementary Movie 4 provide instructions for using the local software *ITK-SNAP-CVE* and online website <https://bcc.ee.cityu.edu.hk/cmos/embSAM> to browse the *EmbSAM* dataset respectively.

## Code availability

Cell lineage tracing is conducted on public *StarryNite* (<https://doi.org/10.1038/nprot.2006.222>), *AceTree* (<https://doi.org/10.1186/1471-2105-7-275>), and *Python* (3.11.0). The *Python* (3.11.0) code for *EmbSAM* framework, including cell shape reconstruction, calculating cell volume, cell surface area, and cell-cell contact relationship and area from segmented 3D cell regions, and generating figures, is reposed at *GitHub* and *Google Colab*, accessible via <https://doi.org/10.6084/m9.figshare.29064530>.

Received: 22 October 2024; Accepted: 11 November 2025;  
Published online: 24 December 2025

## References

1. Rawlinson, K. A. Embryonic and post-embryonic development of the polyclad flatworm *Maritigrella crozieri*; implications for the evolution of spiralian life history traits. *Front. Zool.* **7**, 12 (2010).
2. Truman, J. W. The evolution of insect metamorphosis. *Curr. Biol.* **29**, R1252–R1268 (2019).
3. Xu, B. et al. Unifying developmental programs for embryonic and post-embryonic neurogenesis in the zebrafish retina. *Development* **147**, dev185660 (2020).
4. Pohl, C. & Bao, Z. Chiral forces organize left-right patterning in *C. elegans* by uncoupling midline and anteroposterior axis. *Dev. Cell* **19**, 402–412 (2010).
5. Moerman, D. G., Hutter, H., Mullen, G. P. & Schnabel, R. Cell autonomous expression of perlecan and plasticity of cell shape in embryonic muscle of *Caenorhabditis elegans*. *Dev. Biol.* **173**, 228–242 (1996).
6. Guan, G., Zhao, Z. & Tang, C. Delineating mechanisms and design principles of *Caenorhabditis elegans* embryogenesis using *in toto* high-resolution imaging data and computational modeling. *Comput. Struct. Biotechnol. J.* **20**, 5500–5515 (2022).
7. Lovegrove, H. E. et al. Interphase cell morphology defines the mode, symmetry, and outcome of mitosis. *Science* **388**, eadu9628 (2025).
8. Cao, J. et al. Establishment of a morphological atlas of the *Caenorhabditis elegans* embryo using deep-learning-based 4D segmentation. *Nat. Commun.* **11**, 6254 (2020).
9. Kuang, X. et al. Computable early *Caenorhabditis elegans* embryo with a phase field model. *PLoS Comput. Biol.* **18**, e1009755 (2022).
10. Sugioka, K. & Bowerman, B. Combinatorial contact cues specify cell division orientation by directing cortical myosin flows. *Dev. Cell* **46**, 257–270 (2018).
11. Pimpale, L. G., Middelkoop, T. C., Mietke, A. & Grill, S. W. Cell lineage-dependent chiral actomyosin flows drive cellular rearrangements in early *Caenorhabditis elegans* development. *eLife* **9**, e54930 (2020).
12. Middelkoop, T. C. et al. A cytokinetic ring-driven cell rotation achieves Hertwig's rule in early development. *Proc. Natl. Acad. Sci. USA* **121**, e2318838121 (2024).
13. Fickentscher, R., Krauss, S. W. & Weiss, M. Anti-correlation of cell volumes and cell-cycle times during the embryogenesis of a simple model organism. *New J. Phys.* **20**, 113001 (2018).
14. Fickentscher, R. & Weiss, M. Physical determinants of asymmetric cell divisions in the early development of *Caenorhabditis elegans*. *Sci. Rep.* **7**, 9369 (2017).
15. Azuma, Y., Okada, H. & Onami, S. Systematic analysis of cell morphodynamics in *C. elegans* early embryogenesis. *Front. Bioinform.* **3**, 1082531 (2023).
16. Sobral, M., Sampedro, L., Neylan, I., Siemens, D. & Dirzo, R. Phenotypic plasticity in plant defense across life stages: inducibility, transgenerational induction, and transgenerational priming in wild radish. *Proc. Natl. Acad. Sci. USA* **118**, e2005865118 (2021).
17. Cao, J. et al. CShaperApp: segmenting and analyzing cellular morphologies of the developing *Caenorhabditis elegans* embryo. *Quant. Biol.* **12**, 329–334 (2024).
18. Sulston, J. E., Schierenberg, E., White, J. G. & Thomson, J. N. The embryonic cell lineage of the nematode *Caenorhabditis elegans*. *Dev. Biol.* **100**, 64–119 (1983).
19. Ho, V. W. S. et al. Systems-level quantification of division timing reveals a common genetic architecture controlling asynchrony and fate asymmetry. *Mol. Syst. Biol.* **11**, 814 (2015).
20. Guan, G. et al. System-level quantification and phenotyping of early embryonic morphogenesis of *Caenorhabditis elegans*. Preprint at *bioRxiv* <https://www.biorxiv.org/content/10.1101/776062v1> (2019).
21. Guan, G., Wong, M.-K., Zhao, Z., Tang, L. H. & Tang, C. Volume segregation programming in a nematode's early embryogenesis. *Phys. Rev. E* **104**, 054409 (2021).
22. Packer, J. S. et al. A lineage-resolved molecular atlas of *C. elegans* embryogenesis at single-cell resolution. *Science* **365**, eaax1971 (2019).
23. Ma, X. et al. A 4D single-cell protein atlas of transcription factors delineates spatiotemporal patterning during embryogenesis. *Nat. Methods* **18**, 893–902 (2021).
24. Wang, Z., Xu, Y., Wang, D., Yang, J. & Bao, Z. Hierarchical deep reinforcement learning reveals a modular mechanism of cell movement. *Nat. Mach. Intell.* **4**, 73–83 (2022a).
25. Thiels, W., Smeets, B., Cuvelier, M., Caroti, F. & Jelier, R. spheresDT/Mpacts-PiCS: Cell tracking and shape retrieval in membrane-labeled embryos. *Bioinformatics* **37**, 4851–4856 (2021).
26. Soliman, K. CellProfiler: novel automated image segmentation procedure for super-resolution microscopy. *Biol. Proced. Online* **17**, 11 (2015).
27. Stegmaier, J. et al. Real-time three-dimensional cell segmentation in large-scale microscopy data of developing embryos. *Dev. Cell* **36**, 225–240 (2016).
28. Wang, W. et al. Learn to segment single cells with deep distance estimator and deep cell detector. *Comput. Biol. Med.* **108**, 133–141 (2019).
29. Dosovitskiy, A. et al. An image is worth 16x16 words: transformers for image recognition at scale. *International Conference on Learning Representations (ICLR)*, OpenReview.net (2021).
30. Kirillov, A. et al. Segment Anything. *IEEE/CVF International Conference on Computer Vision (ICCV)* (IEEE 2023).
31. Ding, L. et al. Adapting Segment Anything Model for change detection in VHR remote sensing images. *IEEE Trans. Geosci. Remote Sens.* **62**, 5611711 (2024).
32. Lei, W., Xu, W., Li, K., Zhang, X. & Zhang, S. MedLSAM: Localize and segment anything model for 3D CT images. *Med. Image Anal.* **99**, 103370 (2025).
33. Ma, J. et al. Segment anything in medical images. *Nat. Commun.* **15**, 654 (2024). Software URL: <https://github.com/bowang-lab/MedSAMslicer.git>; Code URL: <https://github.com/bowang-lab/MedSAM>.
34. Wolny, A. et al. Accurate and versatile 3D segmentation of plant tissues at cellular resolution. *eLife* **9**, e57613 (2020).

35. Fabrèges, D. et al. Temporal variability and cell mechanics control robustness in mammalian embryogenesis. *Science* **386**, eadh1145 (2024).

36. Richards, J. L., Zacharias, A. L., Walton, T., Burdick, J. T. & Murray, J. I. A quantitative model of normal *Caenorhabditis elegans* embryogenesis and its disruption after stress. *Dev. Biol.* **374**, 12–23 (2013).

37. Li, X. et al. Systems properties and spatiotemporal regulation of cell position variability during embryogenesis. *Cell Rep.* **26**, 313–321 (2019).

38. Jelier, R., Kruger, A., Swoger, J., Zimmermann, T. & Lehner, B. Compensatory cell movements confer robustness to mechanical deformation during embryonic development. *Cell Syst.* **3**, 160–171 (2016).

39. Azuma, Y. & Onami, S. Biologically constrained optimization based cell membrane segmentation in *C. elegans* embryos. *BMC Bioinform.* **18**, 307 (2017).

40. Guan, G. et al. Cell lineage-resolved embryonic morphological map reveals signaling associated with cell fate and size asymmetry. *Nat. Commun.* **16**, 3700 (2025).

41. Vincent, L. & Soille, P. Watersheds in digital spaces: an efficient algorithm based on immersion simulations. *IEEE Trans. Pattern Anal. Mach. Intell.* **13**, 583–598 (1991).

42. Cao, J., Wong, M.-K., Zhao, Z. & Yan, H. 3DMMS: Robust 3D membrane morphological segmentation of *C. elegans* embryo. *BMC Bioinform.* **20**, 176 (2019).

43. Krull, A., Buchholz, T.-O. & Jug, F. Noise2Void - Learning denoising from single noisy images. *IEEE/CVF Conference on Computer Vision and Pattern Recognition (CVPR)* (IEEE, 2019).

44. Weigert, M. et al. Content-aware image restoration: pushing the limits of fluorescence microscopy. *Nat. Methods* **15**, 1090–1097 (2018).

45. Majeed, M., Chien-Po, L. & Oliver, H. Nervous system-wide analysis of all *C. elegans* cadherins reveals neuron-specific functions across multiple anatomical scales. *Sci. Adv.* **11**, eads2852 (2025).

46. Nance, J. & Priess, J. R. Cell polarity and gastrulation in *C. elegans*. *Development* **129**, 387–397 (2002).

47. Nance, J. PAR proteins and the establishment of cell polarity during *C. elegans* development. *BioEssays* **27**, 126–135 (2005).

48. Girard, L. R. et al. WormBook: the online review of *Caenorhabditis elegans* biology. *Nucleic Acids Res.* **35**, D472–D475 (2007).

49. Cooper, G. M. *The Cell: A Molecular Approach* (2nd edition) – *The Nucleus during Mitosis* (Sunderland (MA): Sinauer Associates, 2000). <https://www.ncbi.nlm.nih.gov/books/NBK9890>.

50. Bao, Z. et al. Automated cell lineage tracing in *Caenorhabditis elegans*. *Proc. Natl. Acad. Sci. USA* **103**, 2707–2712 (2006).

51. Boyle, T. J., Bao, Z., Murray, J. I., Araya, C. L. & Waterston, R. H. AceTree: A tool for visual analysis of *Caenorhabditis elegans* embryogenesis. *BMC Bioinform.* **7**, 275 (2006).

52. Murray, J. I., Bao, Z., Boyle, T. J. & Waterston, R. H. The lineage of fluorescently-labeled *Caenorhabditis elegans* embryos with StarryNite and AceTree. *Nat. Protoc.* **1**, 1468–1476 (2006).

53. Thorpe, C. J., Schlesinger, A., Carter, J. C. & Bowerman, B. Wnt signaling polarizes an early *C. elegans* blastomere to distinguish endoderm from mesoderm. *Cell* **90**, 695–705 (1997).

54. Rocheleau, C. E. et al. Wnt signaling and an APC-related gene specify endoderm in early *C. elegans* embryos. *Cell* **90**, 707–716 (1997).

55. Sanger, J. M., Reingold, A. M. & Sanger, J. W. Cell surface changes during mitosis and cytokinesis of epithelial cells. *Cell Tissue Res.* **237**, 409–417 (1984).

56. Tanaka, M., Fujimoto, K. & Yumura, S. Regulation of the total cell surface area in dividing *Dictyostelium* cells. *Front. Cell Dev. Biol.* **8**, 238 (2020).

57. Guan, G., Chen, Y., Wang, H., Ouyang, Q. & Tang, C. Characterizing cellular physiological states with three-dimensional shape descriptors for cell membranes. *Membranes* **14**, 137 (2024).

58. Guan, G., Kuang, X., Tang, C. & Zhang, L. Comparison between phase-field model and coarse-grained model for characterizing cell-resolved morphological and mechanical properties in a multicellular system. *Commun. Nonlinear Sci. Numer. Simul.* **117**, 106966 (2023).

59. Fujii, Y. et al. Spatiotemporal dynamics of single cell stiffness in the early developing ascidian chordate embryo. *Commun. Biol.* **4**, 341 (2021).

60. Goldstein, B. & Hird, S. N. Specification of the anteroposterior axis in *Caenorhabditis elegans*. *Development* **122**, 1467–1474 (1996).

61. Motegi, F. et al. Microtubules induce self-organization of polarized PAR domains in *Caenorhabditis elegans* zygotes. *Nat. Cell Biol.* **13**, 1361–1367 (2011).

62. Dutta, P., Odedra, D. & Pohl, C. Planar asymmetries in the *C. elegans* embryo emerge by differential retention of aPARs at cell-cell contacts. *Front. Cell Dev. Biol.* **7**, 209 (2019).

63. Arata, Y., Takagi, H., Sako, Y. & Sawa, H. Power law relationship between cell cycle duration and cell volume in the early embryonic development of *Caenorhabditis elegans*. *Front. Physiol.* **5**, 529 (2015).

64. Fickentscher, R., Strutz, P. & Weiss, M. Setting the clock for fail-safe early embryogenesis. *Phys. Rev. Lett.* **117**, 188101 (2016).

65. Kajita, A., Yamamura, M. & Kohara, Y. Physical modeling of the cellular arrangement in *C. elegans* early embryo: effect of rounding and stiffening of the cells. *Genome Inform.* **13**, 224–232 (2002).

66. Kajita, A., Yamamura, M. & Kohara, Y. Computer simulation of the cellular arrangement using physical model in early cleavage of the nematode *Caenorhabditis elegans*. *Bioinformatics* **19**, 704–716 (2002).

67. Pohl, C. Left-right patterning in the *C. elegans* embryo: unique mechanisms and common principles. *Commun. Integr. Biol.* **4**, 34–40 (2011).

68. Fickentscher, R., Ozawa, T., Kimura, A. & Weiss, M. Dynamic allometry of nuclei in early embryos of *Caenorhabditis elegans*. *Phys. Rev. X* **14**, 011016 (2024).

69. Cao, Y. et al. Cell motility dependence on adhesive wetting. *Soft Matter* **15**, 2043–2050 (2019a).

70. Cao, Y., Ghabache, E. & Rappel, W.-J. Plasticity of cell migration resulting from mechanochemical coupling. *eLife* **8**, e48478 (2019b).

71. Ajduk, A. & Zernicka-Goetz, M. Polarity and cell division orientation in the cleavage embryo: from worm to human. *Mol. Hum. Reprod.* **22**, 691–703 (2016).

72. Yushkevich, P. A., Gao, Y. & Gerig, G. ITK-SNAP: An interactive tool for semi-automatic segmentation of multi-modality biomedical images. *Annual International Conference of the IEEE Engineering in Medicine and Biology Society (EMBC)* (IEEE, 2016).

73. van Bavel, C., Thiels, W. & Jelier, R. Cell shape characterization, alignment, and comparison using FlowShape. *Bioinformatics* **39**, btad076 (2023).

74. Hsu, T.-G. et al. Mechanochimically accessing a challenging-to-synthesize depolymerizable polymer. *Nat. Commun.* **14**, 225 (2023).

75. Göbel, V., Barrett, P. L., Hall, D. H. & Fleming, J. T. Lumen morphogenesis in *C. elegans* requires the membrane-cytoskeleton linker *erm-1*. *Dev. Cell* **6**, 865–873 (2004).

76. MacQueen, A. J. et al. ACT-5 is an essential *Caenorhabditis elegans* actin required for intestinal microvilli formation. *Mol. Biol. Cell* **16**, 3247–3259 (2005).

77. Ma, R., Laan, L., Dogterom, M., Pavin, N. & Jülicher, F. General theory for the mechanics of confined microtubule asters. *New J. Phys.* **16**, 013018 (2014).

78. Cuvelier, M. et al. Stability of asymmetric cell division: A deformable cell model of cytokinesis applied to *C. elegans*. *Biophys. J.* **122**, 1858–1867 (2023).

79. Ichbiah, S. et al. Embryo mechanics cartography: inference of 3D force atlases from fluorescence microscopy. *Nat. Methods* **20**, 1989–1999 (2023).

80. Xu, M., Wu, Y., Shroff, H., Wu, M. & Mani, M. A scheme for 3-dimensional morphological reconstruction and force inference in the early *C. elegans* embryo. *PLoS ONE* **13**, e0199151 (2018).

81. Yamamoto, K. et al. Dissecting the subcellular forces sculpting early *C. elegans* embryos. Preprint at *bioRxiv* <https://www.biorxiv.org/content/10.1101/2023.03.07.531437v1> (2023).

82. Yamamoto, K. & Kimura, A. An asymmetric attraction model for the diversity and robustness of cell arrangement in nematodes. *Development* **144**, 4437–4449 (2017).

83. Fujita, M. & Onami, S. Cell-to-cell heterogeneity in cortical tension specifies curvature of contact surfaces in *Caenorhabditis elegans* embryos. *PLoS ONE* **7**, e30224 (2012).

84. Hubatsch, L. et al. A cell-size threshold limits cell polarity and asymmetric division potential. *Nat. Phys.* **15**, 1075–1085 (2019).

85. Guignard, L. et al. Contact area-dependent cell communication and the morphological invariance of ascidian embryogenesis. *Science* **369**, eaar5663 (2020).

86. Khan, Z., Wang, Y.-C., Wieschaus, E. F. & Kaschube, M. Quantitative 4D analyses of epithelial folding during *Drosophila* gastrulation. *Development* **141**, 2895–2900 (2014).

87. Chen, L. et al. Establishment of signaling interactions with cellular resolution for every cell cycle of embryogenesis. *Genetics* **209**, 37–49 (2018).

88. Li, Z. et al. Volume tells: Dual cycle-consistent diffusion for 3D fluorescence microscopy de-noising and super-resolution. *Computer Vision and Pattern Recognition Conference (CVPR)* (IEEE, 2025).

89. Brenner, S. The genetics of behaviour. *Br. Med. Bull.* **29**, 269–271 (1973).

90. Cao, J. et al. Establishment of a morphological atlas of the *Caenorhabditis elegans* embryo using deep-learning-based 4D segmentation. *figshare*, <https://doi.org/10.6084/m9.figshare.12839315> (2020).

91. Santella, A., Du, Z., Nowotschin, S., Hadjantonakis, A.-K. & Bao, Z. A hybrid blob-slice model for accurate and efficient detection of fluorescence labeled nuclei in 3D. *BMC Bioinform.* **11**, 580 (2010).

92. Santella, A., Du, Z. & Bao, Z. A semi-local neighborhood-based framework for probabilistic cell lineage tracing. *BMC Bioinform.* **15**, 217 (2014).

93. Katzman, B., Tang, D., Santella, A. & Bao, Z. AceTree: A major update and case study in the long term maintenance of open-source scientific software. *BMC Bioinform.* **19**, 121 (2018).

94. Schnabel, R., Hutter, H., Moerman, D. & Schnabel, H. Assessing normal embryogenesis in *Caenorhabditis elegans* using a 4D microscope: Variability of development and regional specification. *Dev. Biol.* **184**, 234–265 (1997).

95. Bischoff, M. & Schnabel, R. Global cell sorting is mediated by local cell-cell interactions in the *C. elegans* embryo. *Dev. Biol.* **294**, 432–444 (2006).

96. Guan, G. et al. Cell lineage-resolved embryonic morphological map reveals signaling associated with cell fate and size asymmetry. *figshare*, <https://doi.org/10.6084/m9.figshare.24768921> (2025).

97. Schindelin, J. et al. Fiji: An open-source platform for biological-image analysis. *Nat. Methods* **9**, 676–682 (2012).

98. Audhya, A. et al. A complex containing the Sm protein CAR-1 and the RNA helicase CGH-1 is required for embryonic cytokinesis in *Caenorhabditis elegans*. *J. Cell Biol.* **171**, 267–279 (2005).

99. Matsumura, F. Regulation of myosin II during cytokinesis in higher eukaryotes. *Trends Cell Biol.* **15**, 371–377 (2005).

100. Lan, H. et al. An extracellular matrix protein promotes anillin-dependent processes in the *Caenorhabditis elegans* germline. *Life Sci. Alliance* **2**, e201800152 (2019).

101. Wang, Y. et al. Low-light image enhancement with normalizing flow. *AAAI Conf. Artif. Intell.* **36**, 2604–2612 (2022b).

102. Abdelhamed, A., Brubaker, M. A. & Brown, M. S. Noise flow: Noise modeling with conditional normalizing flows. *IEEE/CVF International Conference on Computer Vision (CVPR)* (IEEE, 2019).

103. Winkler, C., Worrall, D., Hoogeboom, E. & Welling, M. Learning likelihoods with conditional normalizing flows. Preprint at *arXiv* <https://arxiv.org/abs/1912.00042> (2019).

104. Wei, C., Wang, W., Yang, W. & Liu, J. Deep retinex decomposition for low-light enhancement. *British Machine Vision Conference (BMVC)* (The British Machine Vision Association, 2018).

105. Wang, X. et al. ESRGAN: Enhanced super-resolution generative adversarial networks. *European Conference on Computer Vision Workshops (ECCVW)* (Springer, 2018).

106. Otsu, N. A threshold selection method from gray-level histograms. *IEEE Trans. Syst. Man Cybern.* **9**, 62–66 (1979).

107. van der Walt, S. et al. scikit-image: image processing in Python. *PeerJ* **2**, e453 (2014).

108. Douglas, D. H. & Peucker, T. K. Algorithms for the reduction of the number of points required to represent a digitized line or its caricature. *Cartographica* **10**, 112–122 (1973).

109. Huttenlocher, D. P., Klanderman, G. A. & Rucklidge, W. J. Comparing images using the Hausdorff distance. *IEEE Trans. Pattern Anal. Mach. Intell.* **15**, 850–863 (1993).

110. Taha, A. A. & Hanbury, A. Metrics for evaluating 3D medical image segmentation: analysis, selection, and tool. *BMC Med. Imaging* **15**, 29 (2015).

111. Wadell, H. Volume, shape, and roundness of rock particles. *J. Geol.* **40**, 443–451 (1932).

112. Cruz-Matías, I. et al. Sphericity and roundness computation for particles using the extreme vertices model. *J. Comput. Sci.* **30**, 28–40 (2019).

113. Hayakawa, Y. & Oguchi, T. Evaluation of gravel sphericity and roundness based on surface-area measurement with a laser scanner. *Comput. Geosci.* **31**, 735–741 (2005).

114. Zhao, M. et al. Segmentation and classification of two-channel *C. elegans* nucleus-labeled fluorescence images. *BMC Bioinform.* **18**, 412 (2017).

115. Yu, H., Lim, K. P., Xiong, S., Tan, L. P. & Shim, W. Functional morphometric analysis in cellular behaviors: shape and size matter. *Adv. Healthc. Mater.* **2**, 1188–1197 (2013).

116. Lobo, J., See, E. Y.-S., Biggs, M. & Pandit, A. An insight into morphometric descriptors of cell shape that pertain to regenerative medicine. *J. Tissue Eng. Regen. Med.* **10**, 539–553 (2016).

117. Taneja, N. et al. Precise tuning of cortical contractility regulates cell shape during cytokinesis. *Cell Rep.* **31**, 107477 (2020).

118. Fernandez, R. et al. Imaging plant growth in 4D: robust tissue reconstruction and lineaging at cell resolution. *Nat. Methods* **7**, 547–553 (2010).

119. Xiao, L., Fan, D., Qi, H., Cong, Y. & Du, Z. Defect-buffering cellular plasticity increases robustness of metazoan embryogenesis. *Cell Syst.* **13**, 615–630 (2022).

## Acknowledgements

We would like to thank Dr. Yu Chung Tse and Dr. Xiangchuan Wang from SUSTech Core Research Facilities at Southern University of Science and Technology and Prof. Chuanfu Dong at Beijing Normal University for providing technical support on spinning disk confocal imaging as well as the comparison of fluorescence patterns between wild-type and RNAi-treated *C. elegans* embryos with various markers. We are grateful to Yiming Ma at

Hong Kong Baptist University for her invaluable assistance in collecting embryo data. We extend our gratitude to Dr. Dongying Xie and Gefei Huang at Hong Kong Baptist University for the fruitful discussion. This work was supported by the General Research Funds (12101522, 12100024, 12101323) from the Hong Kong Research Grants Council, Hong Kong Innovation and Technology Fund (GHP/176/21SZ), Initiation Grant for Faculty Niche Research Areas (RC-FNRA-IG/21-22/SCI/02), Seed Fund for Collaborative Research (RC-SFCRG/24-25/R1/SCI/01) from Hong Kong Baptist University to Zhongying Zhao, by the National Natural Science Foundation of China (12090053, 32088101) to Chao Tang, by Hong Kong Innovation and Technology Commission (InnoHK Project CIMDA) and Hong Kong Research Grants Council (11204821) to Hong Yan, and by the National Natural Science Foundation of China (22477010, 22407016) to Pei Zhang.

### Author contributions

G.G. and C.Z. devised *EmbSAM* framework. G.G., C.Z., and Z.L. performed quantitative analyses. C.Z. and Z.L. standardized *EmbSAM* dataset for public release. Y.C. applied 3D shape descriptors. P.Z. provided worm images with alternative fluorescent markers, developmental stages, genetic backgrounds, and imaging intervals for preliminary tests. P.Y. constructed *CMOS/EmbSAM* website. M.-K.W. and L.-Y.C. provided worm images with cell lineage tracing. P.Z., H.Y., C.T., and Z.Z. offered financial support. G.G. and Z.Z. conceived the project and wrote and revised the paper.

### Competing interests

The authors declare no competing interests.

### Additional information

**Supplementary information** The online version contains supplementary material available at <https://doi.org/10.1038/s42003-025-09220-3>.

**Correspondence** and requests for materials should be addressed to Guoye Guan or Zhongying Zhao.

**Peer review information** *Communications Biology* thanks Léo Guignard who co-reviewed with Alice Gros, Anthony Santella, and the other, anonymous, reviewer(s) for their contribution to the peer review of this work. Primary Handling Editors: Kaliya Georgieva.

**Reprints and permissions information** is available at <http://www.nature.com/reprints>

**Publisher's note** Springer Nature remains neutral with regard to jurisdictional claims in published maps and institutional affiliations.

**Open Access** This article is licensed under a Creative Commons Attribution-NonCommercial-NoDerivatives 4.0 International License, which permits any non-commercial use, sharing, distribution and reproduction in any medium or format, as long as you give appropriate credit to the original author(s) and the source, provide a link to the Creative Commons licence, and indicate if you modified the licensed material. You do not have permission under this licence to share adapted material derived from this article or parts of it. The images or other third party material in this article are included in the article's Creative Commons licence, unless indicated otherwise in a credit line to the material. If material is not included in the article's Creative Commons licence and your intended use is not permitted by statutory regulation or exceeds the permitted use, you will need to obtain permission directly from the copyright holder. To view a copy of this licence, visit <http://creativecommons.org/licenses/by-nc-nd/4.0/>.

© The Author(s) 2025